Geological Society of America Bulletin

Interaction between deformation and magma extraction in migmatites: Examples from Kangaroo Island, South Australia

Roberto F. Weinberg, Pavlína Hasalová, Lindsay Ward and C. Mark Fanning

Geological Society of America Bulletin 2013;125, no. 7-8;1282-1300
doi: 10.1130/B30781.1

Interaction between deformation and magma extraction in migmatites: Examples from Kangaroo Island, South Australia

Roberto F. Weinberg[1,†], Pavlína Hasalová[1,2,§], Lindsay Ward[1], and C. Mark Fanning[3]
[1]*School of Geosciences, Monash University, Clayton, VIC 3800, Australia*
[2]*Centre for Lithospheric Research, Czech Geological Survey, Klárov 3, 118 21, Prague 1, Czech Republic*
[3]*Research School of Earth Sciences, The Australian National University, Canberra, ACT 0200, Australia*

ABSTRACT

Migmatite terranes are structurally complex because of strong rheological contrast between layers with different melt contents and because of magma migration leading to irregular volume changes. Migmatite deformation is intimately linked with magma extraction and the origin of granitoids. We investigate here the relationships between evolving deformation and magma extraction in migmatites formed during the ca. 500 Ma Delamerian orogeny, exposed on Kangaroo Island, South Australia. Here, several phases of deformation occurred in the presence of melt. During an early upright, noncylindrical folding event, magma was channeled toward the hinge zones of antiforms. Funnel-shaped networks of leucosomes formed a root zone that linked up toward a central axial planar channel, forming the main magma extraction paths during folding. Extraction was associated with fold limb collapse, and antiformal hinge disruption by magma accumulation and transfer. During a later deformation phase, melt-rich diatexites were deformed, and schollen, blocks or rafts of source rock, were disaggregated into smaller blocks and schlieren, and these were deformed into asymmetric, sigmoidal shapes indicative of dextral shearing flow. During flow, magma accumulated preferentially along shear planes, indicating a dilational component during shearing (transtension) and in strain shadows of schollen. At the waning stages of deformation, magma extraction from these diatexites gave rise to N-trending, steeply dipping, funnel-shaped channels not associated with any externally imposed deformational feature. The funnel shape of these structures indicates the direction of magma flow. Structures developed during this phase are comparable with those formed during dewatering of soft sediments. Despite a high degree of complexity, magma migration and extraction features record distinct responses to the evolving deformation that can be used to understand deformation, and the nature and direction of magma extraction. The oldest and youngest magmatic rocks from migmatites were dated by U-Pb SHRIMP (sensitive high-resolution ion microprobe) dating techniques. Both reveal a continuous age spread between ca. 495 and 465 Ma. The age range is interpreted to indicate the duration of anatexis (order of 30 m.y.), with the older ages marking onset of monazite growth as the system approached peak metamorphism and younger ages representing final growth close to the solidus during cooling.

INTRODUCTION

Deformation of anatectic terranes is characterized by structural complexities related to significant competency contrasts and heterogeneous volume changes caused by magma flow in response to pressure gradients across all relevant scales (McLellan, 1988; Davidson et al., 1994; Brown et al., 1995). These complexities lead to atypical structures that make migmatites challenging to decipher. Nevertheless, understanding the evolution of anatectic terranes is a key element in understanding the structural evolution of many terranes (Brown and Solar, 1999), as well as the genesis of crustal magmas and their segregation and extraction from the source (Sawyer, 1998).

Granitic magma migration from its source to form plutons and batholiths is generally associated with contemporaneous deformation (Hollister and Crawford, 1986; Davidson et al., 1994; Collins and Sawyer, 1996; Sawyer, 1996; Brown and Rushmer, 1997; Brown and Solar, 1998a, 1998b; Vigneresse and Burg, 2000; Sawyer, 2001; Vanderhaeghe, 2001, 2009; Weinberg and Mark, 2008; Kruckenberg et al., 2010; McFadden et al., 2010). Pressure gradients arise during continental deformation that adds to magma buoyancy to drive magma migration (Robin, 1979; Sawyer, 1994; Brown et al., 1995; Mancktelow, 2006; Weinberg et al., 2009). The role of melt buoyancy in controlling magma migration has been much debated. At the large scale, melt buoyancy can drive either diapirs (Cruden, 1988; Weinberg and Podlatchikov, 1994; Kruckenberg et al., 2011) or control crack propagation and magma diking through brittle or ductile fracturing of the crust (Lister and Kerr, 1991; Rubin, 1993a, 1993b; Petford et al., 2000; Weinberg and Regenauer-Lieb, 2010). However, at the submillimeter to meter scale, the role of buoyancy is either negligible or obscured by contemporaneous deformation. Compaction as a mechanism for driving melt out of the source (McKenzie, 1984) is thought to be negligible because of the high viscosity of silicic melts (Wickham, 1987; Rabinowicz and Vigneresse, 2004). Instead, melt segregation is thought to be driven by pressure gradients (Robin, 1979; Stevenson, 1989; Sawyer, 1994; Brown et al., 1995; Rutter and Neumann, 1995; Mancktelow, 2006) or by channeling during simple shear (Rabinowicz and Vigneresse, 2004).

The ways in which magma migration and deformation interact vary depending on the nature of the melting process, such as melt reaction, melt production rates, viscosities and permeability evolution, and the nature of deformation and pressure gradients driving magma migration (Clemens and Mawer, 1992; Sawyer, 1994; Rushmer, 2001; Rabinowicz and Vigneresse, 2004; Sawyer and Brown, 2008). This paper contributes to the discussion by investigating the structural evolution of migmatites that formed during anatexis related to the Cambrian Delamerian orogeny exposed

[†]E-mail: roberto.weinberg@monash.edu
[§]Present address: Centre for Lithospheric Research, Czech Geological Survey, Klárov 3, 118 21, Prague 1, Czech Republic.

GSA Bulletin; July/August 2013; v. 125; no. 7/8; p. 1282–1300; doi: 10.1130/B30781.1; 15 figures; 1 table.

in coastal outcrops of the Kanmantoo Group on Kangaroo Island, South Australia. We use these exposures to explore different aspects of magma migration and deformation.

We start with a brief description of the regional geology, followed by a brief overview of the main features of metatexites and diatexites in the region, and a general description of the four main phases of deformation documented in the migmatites. In order to constrain the duration of the anatexis, we present U-Pb SHRIMP ages of monazites. This is then followed by a detailed description of key features that link magma migration and deformation. First, we describe features of magma migration during an early folding event, followed by features developed during oblique normal-dextral shearing. We finish with a description of late- to post-kinematic magma migration with a number of features indicative of magma flow direction, similar to dewatering structures in soft sediments.

REGIONAL GEOLOGY

Kangaroo Island forms part of the Adelaide fold-and-thrust belt and is divided into two main tectonostratigraphic units deformed during the Late Cambrian to Early Ordovician, 514–490 Ma Delamerian orogeny (Foden et al., 2006). The two units are separated by the major E-W–trending Kangaroo Island shear zone (KISZ, Fig. 1). North of the shear zone, an ~1–2-km-thick clastic sedimentary sequence, known as the Kangaroo Island Group (Fig. 1), overlies the Gawler craton (Flöttmann and Cockshell, 1996). South of the shear zone, there is an ~8-km-thick turbiditic, immature graywacke metasedimentary sequence known as the Kanmantoo Group (Fig. 1; Haines et al., 2001), which represents the protolith to the migmatites studied here.

Sedimentation of the Kanmantoo Group began around 522 Ma (Cooper et al., 1992; Jenkins and Sandiford, 1992) and proceeded rapidly (Jago et al., 2003), with the likely sediment source being the eroding uplifted Ross orogen, which had begun ~18 m.y. prior at ca. 540 Ma (Foden et al., 2006). Sedimentation was possibly in a tear basin (Flöttmann et al., 1998) or pull-apart basin (Foden et al., 2006) that formed adjacent to a proposed major shear zone between Australia and Antarctica, which may have separated the Ross and Delamerian orogens during the accretion of Gondwana. Zircon provenance ages support the Ross orogenic belt as the likely sediment source rather than the Proterozoic Gawler craton (Ireland et al., 1998).

The onset of Delamerian orogenic crustal shortening in SE Australia at 514 ± 4 Ma (Foden et al., 1999) terminated Kanmantoo Group sedimentation and initiated basin inversion and the deformation of the Kanmantoo Group, forming what is now the Adelaide fold-and-thrust belt. Crustal convergence resulted in metamorphism and multiple deformation phases. Low-pressure–high-temperature "Buchan-style" peak metamorphism was associated with the first phase of deformation, D_1, reaching upper amphibolite facies (Sandiford et al., 1990), with temperatures up to 650 °C and pressures of 3–4 kbar (Offler and Fleming, 1968; Dymoke and Sandiford, 1992; Sandiford et al., 1995).

Three phases of shortening are recognized in the southern Adelaide fold-and-thrust belt (Offler and Fleming, 1968; Flint and Grady, 1979; Fleming and White, 1984; Mancktelow, 1990; Belperio and Flint, 1993). The first, D_1, resulted in the most widespread effects (Mancktelow, 1990), and, on the island, it gave rise to N-directed thrust faulting and folding and a penetrative, axial-planar S_1 slaty cleavage/schistosity (Flint and Grady, 1979; Belperio et al., 1998).

Flint and Grady (1979) defined D_2, characterized by mesoscopic upright folds and axial planes trending north and northeast. D_3 resulted in NW-SE–trending structures and fabrics that dip steeply to the north (Offler and Fleming,

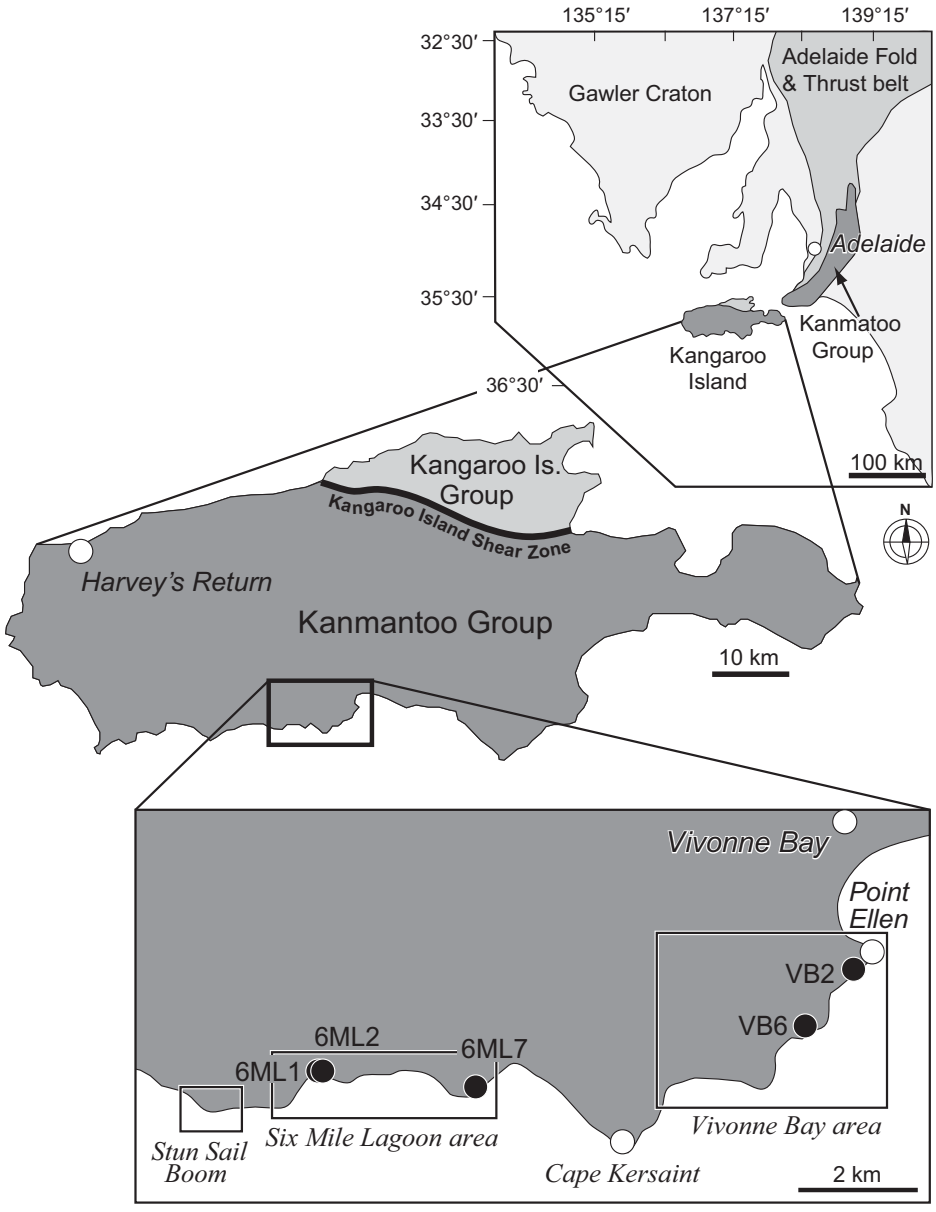

Figure 1. Southern Adelaide fold-and-thrust belt showing the Kanmantoo Group and the field areas on Kangaroo Island, adapted from Yassaghi et al. (2004). Localities mentioned in this study are also shown.

1968; Flint and Grady, 1979). Following the D_3 event, a relaxation of compressive forces with the waning of the Delamerian orogeny was associated with the onset of broadly E-W–directed extension and intrusion of 500 ± 7 Ma (SHRIMP U-Pb analysis of zircons; Fanning, 1990) NW-trending rhyodacite dikes on Kangaroo Island (Foden et al., 2002).

Numerous I- and S-type granitic intrusions of Delamerian age outcrop along the southern coast of Kangaroo Island. Here, a K-feldspar megacrystic granite transitional between I- and S-type was dated at 503 ± 4 Ma (and leucogranite was dated at 504 ± 1 Ma; Fanning, 1990). Leucosomes in migmatites produced in association with these granitic intrusions (Foden et al., 2002) yielded monazite U-Pb LA-ICP-MS (laser ablation–inductively coupled plasma–mass spectrometry) ages of ca. 498–488 Ma, with mean average age of 494 ± 4 Ma (Tassone, 2008), coincident with the waning phases of the Delamerian orogeny and transition from convergent to extensional tectonics (Foden et al., 2006). This transition was followed by a change from syntectonic I- and S-types to undeformed A-type granitic intrusions, which mark the termination of the Delamerian orogeny at around 490 ± 3 Ma (Foden et al., 2002, 2006). The age of peak metamorphism in the Kangaroo Island Group was determined by U-Pb LA-ICP-MS in monazites from an amphibolite-facies metasedimentary rock from Harvey's Return on the northwestern coast of Kangaroo Island (Fig. 1), and it yielded an age of 516 ± 7 Ma (Tassone, 2008).

Melting recorded by the migmatites on the south of the island has been interpreted to be a result of muscovite-dehydration reactions. This interpretation is based on the rare presence of sillimanite, which, when preserved, is surrounded by muscovite, and the extensive presence of randomly oriented muscovite in the migmatites, thought to be a result of retrogression of sillimanite produced during melting (Tassone, 2008). Biotite is apparently stable, and the absence of other peritectic minerals suggests that metamorphic conditions did not reach biotite-dehydration melting reactions at the exposure levels. Garnet is only rarely found and is not peritectic, but it is present in mesosomes reflecting peak amphibolite-facies conditions. Sills of leucogranites in metatexites close to Cape Kersaint (Fig. 1) also contain occasional, up to 10-cm-wide irregular pods of almandine-rich garnet, and it has been suggested that this garnet-leucogranite represents a fractionation product of melt derived from biotite-dehydration melting in unexposed hotter parts of the anatectic terrane (Foden et al., 2002).

RESULTS

On the southern coast of Kangaroo Island there are complex outcrops consisting of a variety of migmatites intruded by granitic dikes and granitic plutons with a variety of modal proportions of minerals and fabrics.

Migmatites

Metatexites are migmatites that remain coherent during melting so that layers preserve continuity. Leucocratic material, typically consisting of granular quartz, plagioclase, and K-feldspar, forms leucosomes and represents a combination of crystallized products from former melt and residual material of the melting reaction. Melanosomes consisting of biotite ± muscovite represent solid material and melting reaction products left behind after melt segregation. Leucosomes with melanocratic borders and diffuse boundaries against the adjacent rock are interpreted to be in situ, whereas those with sharp boundaries and no melanocratic borders are interpreted to be intrusive but still in source. Metatexites on Kangaroo Island are generally stromatic, but patch and network metatexites (Sawyer, 2008) are also found, and leucosomes vary in modal composition from granite to tonalite.

Diatexites are dominated by neosome, or newly formed rock, and they occur where original mesosome/paleosome layers lose continuity and become either isolated blocks in a heterogeneous magmatic rock (schollen), or where they are disaggregated into planar or irregular accumulations of mafic minerals (schlieren) (see Brown, 1973; Sawyer, 2008). Diatexites are typically coarse grained, containing quartz, plagioclase, K-feldspar, biotite, muscovite and tourmaline (neosome). They are compositionally heterogeneous with leucocratic granular patches (leucosomes), biotite and muscovite selvages and pods, forming numerous schollen and schlieren (Fig. 2). Schollen representing different degrees of partially melted Kanmantoo Group rocks have a variety of shapes, sometimes with internal layering parallel to foliation in the surrounding diatexite, and sometimes at high angles to it (Fig. 2). Schollen are commonly deformed, and their asymmetric shapes indicate shear sense (Fig. 2A; Sawyer, 1998). Many larger psammo-pelitic schollen contain ptygmatically folded leucosomes (Figs. 2A and 2B), which generally have narrow melanocratic rims, rich in biotite and indicate a high degree of shortening possibly prior to magma crystallization. Schlieren of biotite and muscovite are common in Kangaroo Island diatexites and are up to 2 cm wide and a few meters long (Figs. 2A and 2D). Diatexites are intruded in places by magmas forming irregular dikes with irregular margins and varying widths, suggesting intrusion while the diatexite was still partially molten (Fig. 2C). Diatexites grade into either metatexite or into enclave-rich granite. The boundary between diatexite and granite is subjective, and following Sawyer (1998), the term granite is used if the neosome texture is uniform (fewer schlieren and inclusions).

Structural Evolution

We documented four deformation events in anatectic rocks on the southern coast of the island (Figs. 3 and 4). Typically, two or more deformation events could be determined in a single outcrop, and their kinematics and relative ages were brought together to define the history of deformation. The deformation phases so determined do not match the ones determined by previous workers on lower-grade metamorphic rocks to the north and described previously herein. All four events were associated with the presence of melt, as evidenced by a continuous link between in situ leucosomes and intrusive leucocratic magma into shear zones and fold hinges. In this section, we present a broad summary of these phases before focusing on magma behavior during deformation.

First Deformation Phase (D_1)

D_1 is generally preserved as small (decimeter-scale) tight to isoclinal folds refolded by and preserved on the limbs of D_2 folds (Figs. 3A and 3B). D_1 folds are associated with a well-developed, intense lineation, L_1, generally plunging gently NNE-SSW and parallel to the F_1 fold axis (Fig. 3A). L_1 is pervasive in metatexites and typically at high angle to F_2 fold axes and is folded by F_2, causing deviations from the original trend (Figs. 3A and 3E).

At Six Mile Lagoon (outcrop 6ML7; 36°01′23.4″S, 137° 05′38.0″E; Fig. 1), there is a 50-m-wide zone of diatexite characterized by subvertical foliation defined by schlieren and aligned schollen, striking NW (~300°). In amongst the schollen, there are isoclinal, rootless fold hinges. This zone is in irregular, partly conformable contact with metatexites interlayered with diatexites to the east. The metatexites have the same attitude, but they are overprinted by narrow, thrust planes trending ~050°/20–30°N, containing leucosomes (Fig. 3C) and associated with isoclinal, recumbent folds. These deflect migmatite layering into parasitic, asymmetric folds with axial-planar leucosomes (Fig. 3D).

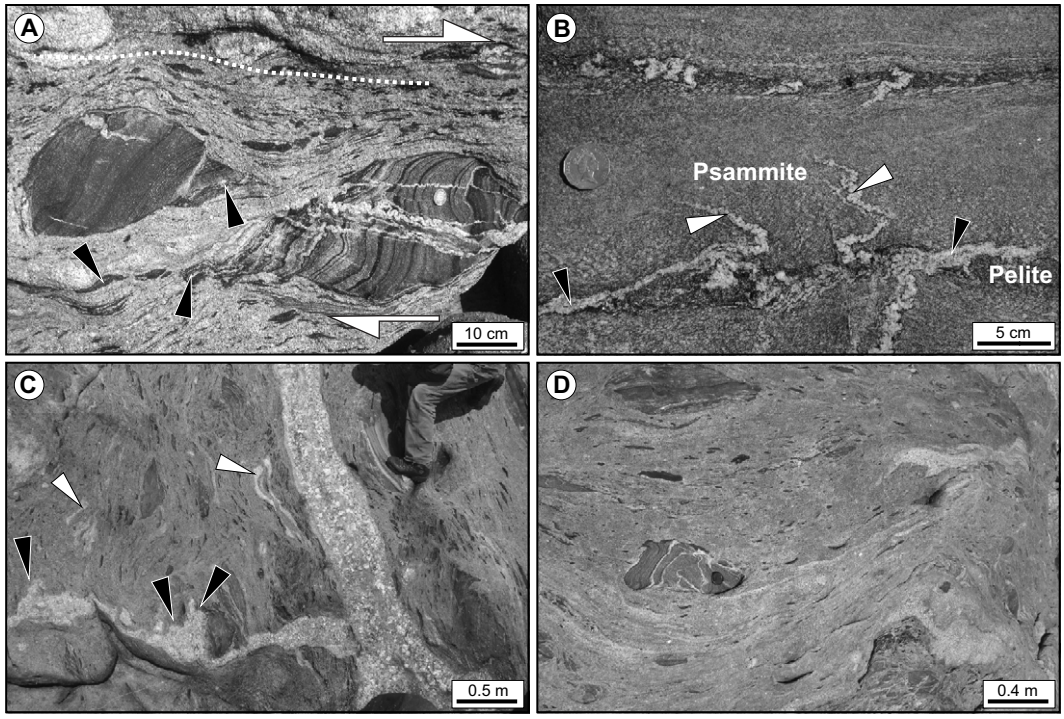

Figure 2. Characteristic features of diatexites: (A) Schollen of layered Kanmantoo Group turbidites with leucocratic ptygmatic veins. Schollen have been deformed as indicated by dragged margins. Asymmetry indicates top-to-the-right shearing in plane of photograph. Surrounding diatexite is intensely foliated (white dashed line); foliation is defined by schlieren and elongated schollen, interpreted to result from disruption of larger schollen (black arrows). (B) Schollen with leucosomes. Psammitic layer, center, fines downward, becoming more biotite-rich, and is separated from a pelitic layer by a sharp boundary. The volume of leucosome increases as the psammite gets finer, and the pelitic layer is more suitable for melting with larger proportion of leucosomes (black arrows). Leucosomes in psammite are ptygmatic (white arrows) and have narrow biotite rims (melanosome). (C) Diatexite intruded by coarse-grained porphyritic leucogranite dike. The dike branches into two at the base of the outcrop. The lower branch, at high angle to foliation, has varying widths and irregular margins, suggesting intrusion into a soft, partially molten surrounding diatexite (black arrows). Note also irregular patches of the same leucogranite in the overlying diatexite (white arrows), suggesting some mingling occurred. (D) Strongly foliated diatexite with interfingered contact between a lighter and a darker diatexite, suggesting interaction between diatexites from different sources. Photo in B is from Six Mile Lagoon area (6ML1), and A, C, and D are from Stun Sail Boom area (in Fig. 1).

The isoclinal folds and the steep, NW-trending diatexite layering and foliation are interpreted to have developed in the earlier part of D_1 deformation, and to have steepened due to strain accumulation. These early structures were then rejuvenated by the development of new D_1 low-angle thrusts with asymmetric folds that allowed for continued shortening. These structures are all kinematically compatible and are overprinted by all other deformation events, and this is why they are interpreted to record the earliest deformation phase affecting the migmatites. The presence of leucosomes in axial-planar orientation in asymmetric folds associated with thrust planes and in the thrust planes themselves (Figs. 3C and 3D) suggests that melt was present during deformation.

We note, however, that the diatexite layering and its steep NW-trending attitude do not provide enough information to define whether they represent an earlier deformation phase or whether they were indeed structures that were part of D_1 that became steepened. We therefore define the first deformation D_1 phase as including the thrusting and asymmetric folding, and we tentatively place the earlier steep foliation and its rootless folds within the same deformation.

Second Deformation Phase (D_2)

D_2 is well preserved in metatexites west of Point Ellen, in Vivonne Bay (outcrop VB2; 35°59′56″S, 137°11′11″E; Fig. 1). Here, it is characterized by open, rounded, and upright folds with wavelengths of 10–15 m and 1 to 2 m amplitude (Fig. 3E). Folds are typically non-cylindrical, with antiforms and synforms merging along the trend of the folds. Folds generally plunge gently to the west and have axial-planar orientation approximately E-W, lacking axial-planar foliation (Fig. 3E). Similar features were found further west (outcrop VB6; 36°00′38.9″S, 137°10′12.6″E; Fig. 1), but here the folds plunge 20–30°ENE. D_2 folds overprint and rotate well-developed L_1 and preserve F_1 isoclinal folds on its limbs (Figs. 3A and 3B). D_2 could potentially be related to the regional D_1 described in the literature, responsible for N-directed thrusting and E-W–trending folds mapped in the northern part of the island (Flint and Grady, 1979).

Third Deformation Phase (D_3)

Rocks folded by D_2 are overprinted by normal shear zones trending N-S, forming a conjugate pair containing leucosomes (Figs. 4A and 4B). This phase is best developed in outcrop VB6 (Fig. 1), where at the outcrop scale, it is represented by a N-trending normal shear zone bending F_2 fold limbs. At the decimeter scale, it is represented by leucosome-filled conjugate shear zones that give rise to centimeter-scale, N-trending ridges on exposed surfaces (Fig. 4A). Combined, these features define an E-W extensional event postdating D_2.

Fourth Deformation Phase (D_4)

D_4 is characterized by dextral-normal shear zones, also filled with leucosomes (Figs. 4C and 4D) and occasionally associated with wide pegmatite intrusions and ~1-m-wide granitic bands containing schlieren. These late structures overprint all previous deformation phases (e.g., D_2 folds, D_3 shear zones in outcrop VB6, and D_1 structures in outcrop 6ML7) and are not overprinted by any later structures. In outcrop VB6, D_4 is characterized by ENE-WSW steep shear zones filled with leucosomes that are continuously linked with layer-parallel, in situ leucosomes, and it is therefore interpreted to be a synmagmatic deformation event. Some D_4 shear zones have a brittle appearance (Fig. 4C), such as described by Davidson et al. (1994). D_4 is responsible for the shearing of the

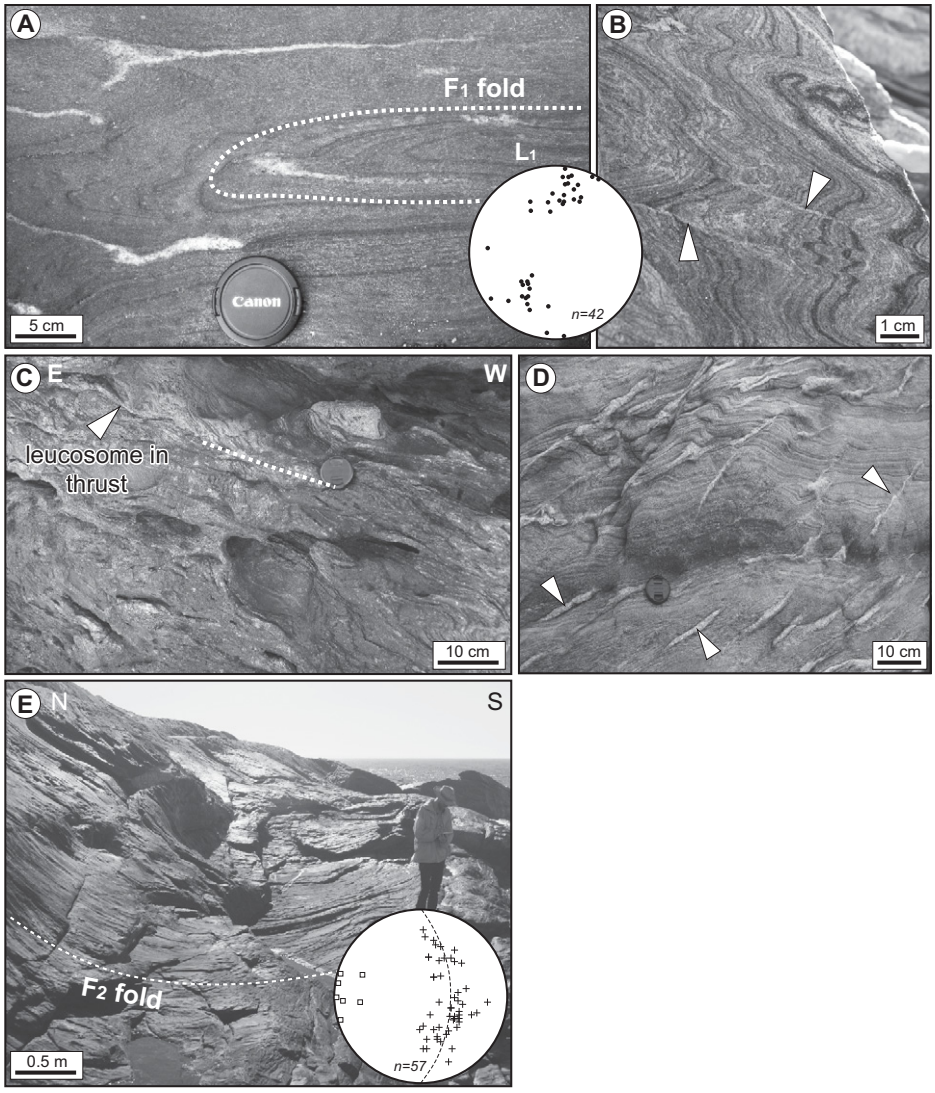

Figure 3. Characteristic D_1 (A–D) and D_2 (E) features: (A) Tight F_1 folds of interlayered psammite-pelite of the Kanmantoo Group in the limb of an F_2 fold in the Vivonne Bay area. (B) Thrust plane with leucosome trending N08°E/38°W (white arrows; locality VB6). Inset: stereonet (equal-area, lower-hemisphere projection) of L_1 lineations, generally oriented NNE-SSW and defining a wide great circle due to folding around F_2 folds. Number of measurements is shown (*n*). (C) Thrust planes (dashed white line) with leucosomes in diatexite trending ~050°/25°NW (locality 6ML7). (D) Asymmetric fold train with leucosome segregated along axial plane (white arrows). (E) Folded S_0 defining a typical F_2 synform. Inset: stereonet (equal-area, lower-hemisphere projection) of poles to bedding (black crosses) and F_2 fold axis (white rectangles) defining westerly gently plunging folds. Number of measurements is shown (*n*).

diatexites in Six Mile Lagoon (outcrop 6ML1; 36°01′19.5″S, 137°03′14.7″E; Fig. 1) described later herein.

U-Pb Monazite Geochronology

In order to constrain the duration of anatexis and to determine the timing of the different anatectic/deformation events, we collected two samples of granitic rock from within the diatexites in Six Mile Lagoon (Fig. 1): one from within the earliest D_1 deformation (sample 6ML7a) and one from the latest D_4 deformation (sample 6ML1a).

Methodology

Each sample was crushed and milled, and monazite grains were separated and mounted in epoxy resin together with monazite 44069 standard (425 ± 1 Ma; Aleinikoff et al., 2006). The mount was then polished. Prior to analysis, all monazite grains were photographed in transmitted and reflected light, as well as imaged by backscattered electrons (BSE) on the scanning electron microscope. This allowed us to identify pristine areas for analysis and to determine if multiple age components (e.g., cores and overgrowths) were present. Monazites were dated using the SHRIMP II at the Research School of Earth Sciences at the Australian National University (ANU). Analytical procedure for monazite dating followed methods described in Williams et al. (1996). The SHRIMP raw data were reduced with SQUID 2 program (Ludwig, 2001; http://sourceforge.net/projects/squid2/files). Isotopic age data for the two samples are given in Table 1; uncertainties given for individual analyses (ratios and ages) are 1σ values.

Results

Monazites from both samples (6ML7a and 6ML1a) are euhedral to round in shape and small, ranging in size from 50 µm to 150 µm (Fig. 5). Monazite grains are either homogeneous, with no zoning visible in BSE, or they have visible concentric to slightly patchy zoning (Figs. 5C and 5F). The latter type is present in the D_1 diatexite sample (6LM7a), in contrast to monazite grains from the D_4 diatexite sample (6ML1a), where the homogeneous grains dominate, and only a few grains reveal core and rim texture (Figs. 5C and 5F). There is no relationship between monazite size and zoning.

All monazite data lie slightly above the concordia, yielding reversely discordant isotope ratios (Figs. 5A and 5C). Reverse discordance is a common feature of U-Pb monazite data and is thought to indicate ^{230}Th disequilibrium (Schärer, 1984; Parrish, 1990; Hawkins and Bowring, 1997). However, reverse discordance is rarely observed in SHRIMP monazite data, and additionally we do not observe any correlation between the degree of discordance and the concentration of either Th or Th/U (Table 1). Therefore, we suggest that reverse discordance resulted from the very high U concentrations in these studied monazites (5000–19,000 ppm; Table 1). Very high U areas, when analyzed by SHRIMP, usually give anomalously old ^{206}Pb/^{238}U ratios/ages because the Pb is preferentially sputtered, and the high U does not match the U of the reference monazite (2500 ppm) used to calibrate the U/Pb ratios (Stern and Berman, 2000; Williams and Hergt, 2000; White and Ireland, 2012). As a consequence, we regard ^{207}Pb/^{206}Pb as the most reliable estimates of the ages of these monazites and use these for further discussion.

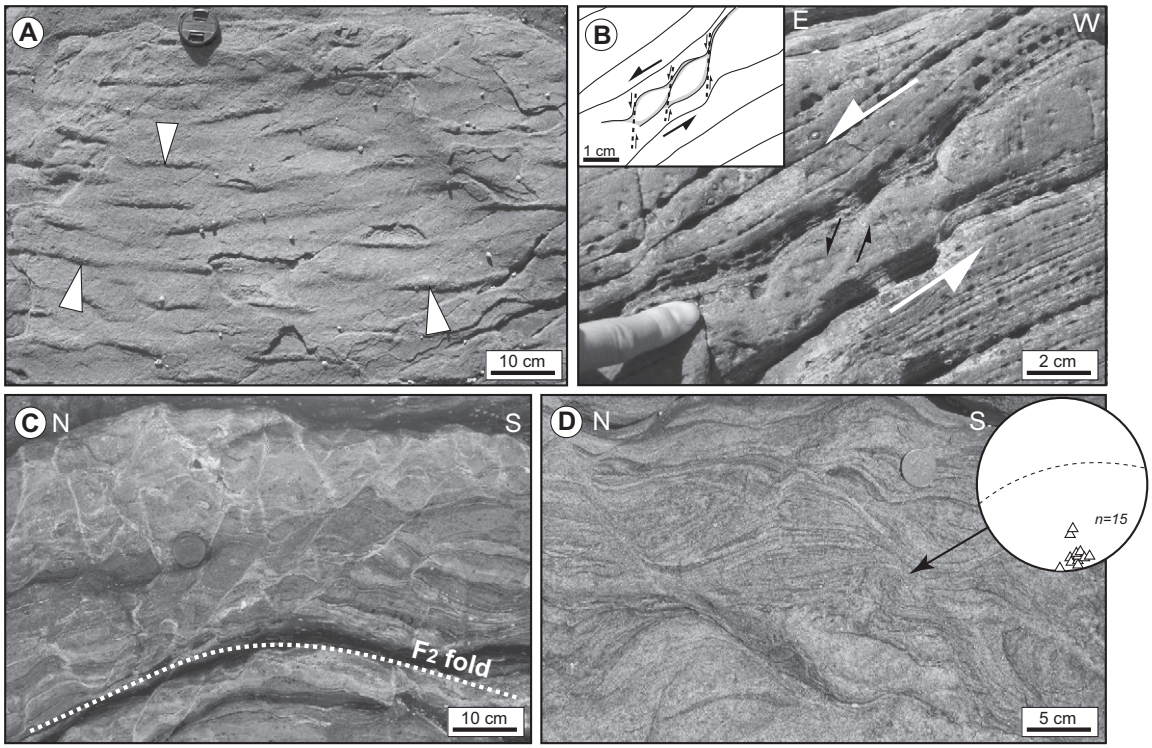

Figure 4. Characteristic D_3 (A–B) and D_4 (C–D) features: (A) Normal shear zones filled with leucosomes forming N-trending ridges on S_0 planes (white arrows). (B) Anastomosing nature of leucosomes defining S-C planes and down-to-the-E movement (see inset). (C) F_2 hinge overprinted by a conjugate set of normal D_4 faults filled with granite. The conjugate set has a brittle appearance. (D) Isoclinal folds, possibly F_1, in stromatic migmatite, overprinted by a conjugate set of normal faults related to D_4. Inset: Stereonet of poles to D_4 shear zones (equal-area, lower-hemisphere projection). Number of measurements is indicated (*n*). Exposure planes on B, C, and D are nearly vertical.

D_1 diatexite (sample 6ML7a). Fourteen spots on five monazites were analyzed in sample 6ML7a. The monazite fraction in this sample was very limited, with only a few grains present, and therefore no more grains could be analyzed. All analyses are slightly reversely discordant ($\bar{x}$disc. % = –5; Fig. 5A; Table 1) and reveal a continuum of single $^{207}Pb/^{206}Pb$ ages from 499 ± 12 Ma to 469 ± 6 Ma (Fig. 5A). The probability density plot shows one broad peak including all data (Fig. 5A). However, all monazite grains reveal zoning, with systematic age differences between their cores and rims (Fig. 5C). Seven monazite rim analyses yield slightly younger $^{207}Pb/^{206}Pb$ ages, between 480 ± 7 Ma and 470 ± 12 Ma (Fig. 5B). The seven monazite core analyses yield $^{207}Pb/^{206}Pb$ ages between 499 ± 12 Ma and 480 ± 10 Ma (Fig. 5B).

D_4 diatexite (sample 6ML1a). Twenty-six spots on 16 mounted monazites were analyzed in sample 6ML1a. All analyses are reversely discordant ($\bar{x}$disc. % = –8; Fig. 5D; Table 1) and reveal a continuum of single $^{207}Pb/^{206}Pb$ ages from 493 ± 6 Ma to 461 ± 5 Ma (Fig. 5D). The high mean square of weighted deviates (MSWD) of 2.7 for all analyses suggests excess scatter, and the probability density plot shows one broad peak including all data (Fig. 5D). As mentioned, only some monazite grains in this sample are zoned. These reveal systematic age differences between cores and rims (Figs. 5E and 5F). We therefore processed core and rim data separately. Importantly, homogeneous monazite grains yield similar ages to the rim ages of zoned monazites (Figs. 5E and 5F); therefore, we decided to further evaluate the two together. In total, 15 rim and homogeneous monazite analyses reveal $^{207}Pb/^{206}Pb$ ages between 479 ± 5 Ma and 461 ± 5 Ma (Fig. 5E). Eight monazite core analyses yield $^{207}Pb/^{206}Pb$ ages between 493 ± 6 Ma and 480 ± 5 Ma (Fig. 5E).

Altogether, both dated samples have a similar extent of continuous ages from ca. 495 Ma to ca. 465 Ma (Fig. 5). The data for each sample can be split into rims and cores defining two slightly different age groups of ca. 495–480 Ma and ca. 480–465 Ma. We suggest that the continuous spread of recorded ages in both samples records the span of anatexis (~30 m.y.) and that the two age ranges reflected in each sample mark the onset of monazite growth (older ages) and then further monazite growth closer to the solidus during cooling. Accordingly, we suggest that any weighted mean calculation would yield an arbitrary mixed date that would not be of any geological significance.

MIGMATITE DEFORMATION AND MAGMA MIGRATION

This section focuses on structures developed during the D_2, D_4, and late- to post-D_4 deformation events, and their relation to magma migration.

D_2 Folding and Axial-Planar Migration

Relationships between D_2 folding and magma migration in metatexites are well exposed west of Vivonne Bay in outcrop VB2 (Figs. 1 and 6). A key feature of these migmatites is that leucosomes form an interconnected network linking layer-parallel leucosomes with in-source

TABLE 1. SUMMARY OF SENSITIVE HIGH-RESOLUTION ION MICROPROBE (SHRIMP) U-Pb MONAZITE RESULTS FOR SAMPLES 6ML7A AND 6ML1A

Grain spot	Position	U (ppm)	Th (ppm)	Th/U	$^{206}Pb^*$ (ppm)	$^{204}Pb/^{206}Pb$	f_{206} %†	Total ratios				Radiogenic ratios						ρ	Age (Ma)				% disc§
								$^{238}U/^{206}Pb$	±	$^{207}Pb/^{206}Pb$	±	$^{206}Pb/^{238}U$	±	$^{207}Pb/^{235}U$	±	$^{207}Pb/^{206}Pb$	±		$^{206}Pb/^{238}U$	±	$^{207}Pb/^{206}Pb$	±	
Sample 6ML7a (D_1 diatexite)																							
1.1	Core	10,911	27,000	2.47	774	0.000010	0.02	12.11	0.15	0.0569	0.0003	0.0826	0.0010	0.6455	0.0086	0.0567	0.0003	0.936	511.4	6.1	480	10	–6
1.2	Rim	3652	46,271	12.67	253	0.000070	0.13	12.38	0.13	0.0575	0.0002	0.0807	0.0009	0.6280	0.0074	0.0565	0.0003	0.895	500.2	5.1	470	12	–6
1.3	Core	9070	23,091	2.55	643	0.000015	0.03	12.12	0.12	0.0571	0.0001	0.0825	0.0008	0.6474	0.0067	0.0569	0.0001	0.986	511.0	5.0	488	4	–5
1.4	Rim	9488	21,530	2.27	667	0.000010	0.02	12.21	0.12	0.0568	0.0002	0.0819	0.0008	0.6398	0.0068	0.0567	0.0002	0.956	507.2	4.9	480	7	–6
2.1	Core	19,501	22,129	1.13	1307	0.000007	0.01	12.82	0.13	0.0572	0.0002	0.0780	0.0008	0.6137	0.0067	0.0571	0.0002	0.954	484.1	4.8	494	7	2
2.2	Rim	5232	35,300	6.75	357	0.000034	0.06	12.59	0.13	0.0570	0.0003	0.0794	0.0008	0.6185	0.0076	0.0565	0.0004	0.848	492.4	4.9	472	14	–4
2.3	Core	6211	45,211	7.28	421	0.000041	0.07	12.68	0.15	0.0573	0.0002	0.0788	0.0009	0.6162	0.0078	0.0567	0.0002	0.942	489.0	5.6	480	9	–2
2.4	Rim	4549	29,242	6.43	328	0.000032	0.06	11.91	0.12	0.0569	0.0001	0.0839	0.0009	0.6527	0.0069	0.0564	0.0001	0.970	519.3	5.1	469	6	–11
5.1	Rim	4957	30,404	6.13	356	0.000026	0.05	11.97	0.12	0.0569	0.0001	0.0835	0.0009	0.6509	0.0068	0.0565	0.0001	0.974	517.1	5.1	473	5	–9
3.1	Core	6062	29,964	4.94	434	0.000043	0.08	11.99	0.12	0.0574	0.0002	0.0834	0.0009	0.6529	0.0072	0.0568	0.0002	0.952	516.1	5.2	484	7	–7
4.1	Rim	4520	30,171	6.68	315	0.000030	0.05	12.31	0.13	0.0570	0.0002	0.0812	0.0008	0.6331	0.0071	0.0566	0.0002	0.930	503.1	5.1	475	9	–6
4.2	Core	2969	36,437	12.27	208	0.000033	0.06	12.25	0.13	0.0577	0.0002	0.0816	0.0009	0.6430	0.0077	0.0572	0.0003	0.895	505.4	5.2	499	12	–1
4.3	Core	6101	23,957	3.93	438	0.000019	0.03	11.98	0.12	0.0571	0.0003	0.0834	0.0008	0.6536	0.0074	0.0568	0.0003	0.902	516.7	5.0	484	11	–7
4.4	Rim	5121	25,543	4.99	356	0.000025	0.04	12.36	0.13	0.0569	0.0001	0.0809	0.0008	0.6303	0.0067	0.0565	0.0001	0.971	501.3	4.9	473	6	–6
Sample 6ML1a (D_4 diatexite)																							
1.1	Rim	10,080	34,232	3.40	706	0.000026	0.05	12.27	0.13	0.0569	0.0001	0.0815	0.0009	0.6350	0.0070	0.0565	0.0002	0.970	504.9	5.2	473	6	–7
1.2	Core	9836	37,544	3.82	687	0.000027	0.05	12.30	0.14	0.0572	0.0001	0.0813	0.0009	0.6363	0.0073	0.0568	0.0002	0.972	503.6	5.4	484	6	–4
2.1	No zoning	8140	32,979	4.05	551	0.000037	0.07	12.69	0.13	0.0572	0.0002	0.0787	0.0008	0.6156	0.0066	0.0567	0.0002	0.958	488.5	4.8	481	7	–2
4.1	No zoning	9012	27,925	3.10	643	0.000033	0.06	12.03	0.13	0.0571	0.0002	0.0831	0.0009	0.6479	0.0074	0.0566	0.0002	0.954	514.3	5.4	475	8	–8
5.1	Core	9403	28,999	3.08	664	0.000014	0.03	12.16	0.12	0.0572	0.0001	0.0822	0.0008	0.6466	0.0068	0.0570	0.0002	0.967	509.4	5.0	493	6	–3
5.2	Rim	6645	25,281	3.80	450	0.000044	0.08	12.69	0.13	0.0572	0.0002	0.0788	0.0008	0.6145	0.0069	0.0566	0.0002	0.922	488.8	4.8	475	10	–3
6.1	No zoning	8356	33,067	3.96	621	0.000029	0.05	11.56	0.12	0.0572	0.0001	0.0865	0.0009	0.6764	0.0070	0.0567	0.0001	0.981	534.5	5.2	482	4	–11
7.1	Core	10,588	30,252	2.86	752	0.000029	0.05	12.10	0.12	0.0573	0.0001	0.0826	0.0008	0.6479	0.0066	0.0569	0.0001	0.987	511.8	5.0	486	4	–5
7.2	Rim	6769	28,402	4.20	481	0.000028	0.05	12.09	0.12	0.0571	0.0001	0.0827	0.0008	0.6461	0.0068	0.0567	0.0001	0.972	512.0	5.0	479	5	–7
8.1	Core	10,506	29,960	2.85	744	0.000018	0.03	12.13	0.12	0.0570	0.0001	0.0824	0.0008	0.6442	0.0067	0.0567	0.0001	0.975	510.4	5.0	480	5	–6
8.2	Rim	10,036	34,274	3.41	695	0.000026	0.05	12.41	0.13	0.0570	0.0002	0.0805	0.0008	0.6284	0.0067	0.0566	0.0002	0.955	499.4	4.9	476	7	–5
9.1	Core	8896	25,097	2.82	743	0.000030	0.05	10.29	0.12	0.0571	0.0002	0.0971	0.0011	0.7587	0.0093	0.0567	0.0002	0.945	597.4	6.6	479	9	–25
9.2	Rim	11,103	35,226	3.17	782	0.000025	0.05	12.19	0.12	0.0568	0.0001	0.0820	0.0008	0.6382	0.0066	0.0565	0.0001	0.986	507.9	4.9	471	4	–8
10.1	Core	8280	24,752	2.99	598	0.000025	0.04	11.89	0.12	0.0572	0.0001	0.0841	0.0009	0.6590	0.0069	0.0568	0.0001	0.988	520.5	5.2	485	4	–7
10.2	Rim	12,235	40,902	3.34	851	0.000031	0.06	12.36	0.13	0.0570	0.0001	0.0809	0.0008	0.6310	0.0066	0.0566	0.0001	0.981	501.4	5.0	475	4	–6
11.1	Rim	7500	26,663	3.56	563	0.000033	0.06	11.45	0.12	0.0568	0.0001	0.0873	0.0009	0.6780	0.0073	0.0563	0.0001	0.987	539.5	5.5	466	4	–16
11.2	Rim	5627	31,069	5.52	401	0.000042	0.07	12.04	0.12	0.0571	0.0001	0.0830	0.0008	0.6467	0.0068	0.0565	0.0001	0.971	513.8	5.0	473	5	–9
12.1	Core	7615	23,608	3.10	569	0.000041	0.07	11.50	0.12	0.0570	0.0001	0.0869	0.0009	0.6763	0.0073	0.0564	0.0001	0.988	537.3	5.5	469	4	–14
12.2	Rim	7745	29,451	3.80	543	0.000065	0.12	12.26	0.12	0.0574	0.0001	0.0815	0.0008	0.6341	0.0066	0.0564	0.0001	0.977	505.1	4.9	469	5	–8
13.1	Core	9857	28,508	2.89	691	0.000019	0.03	12.25	0.12	0.0567	0.0001	0.0816	0.0008	0.6349	0.0065	0.0564	0.0001	0.987	505.5	4.9	470	4	–8
13.2	Rim	9387	27,624	2.94	652	0.000026	0.05	12.37	0.13	0.0566	0.0001	0.0808	0.0008	0.6266	0.0065	0.0562	0.0001	0.979	501.1	4.9	461	5	–9
14.1	No zoning	8494	27,025	3.18	600	0.000026	0.05	12.17	0.12	0.0570	0.0001	0.0821	0.0008	0.6418	0.0066	0.0567	0.0001	0.984	508.9	5.0	478	4	–6
15.1	No zoning	7166	29,430	4.11	499	0.000035	0.06	12.35	0.13	0.0568	0.0003	0.0809	0.0008	0.6283	0.0070	0.0563	0.0003	0.909	501.7	4.9	464	10	–8
16.1	No zoning	8870	32,371	3.65	614	0.000028	0.05	12.42	0.13	0.0569	0.0001	0.0805	0.0008	0.6272	0.0066	0.0565	0.0001	0.973	499.0	4.9	473	5	–6
17.1	No zoning	8729	29,213	3.35	598	0.000023	0.04	12.55	0.13	0.0566	0.0003	0.0797	0.0008	0.6186	0.0071	0.0563	0.0003	0.885	494.2	4.8	464	12	–6
17.2	No zoning	8455	25,264	2.99	617	0.000028	0.05	11.77	0.12	0.0567	0.0001	0.0849	0.0009	0.6590	0.0068	0.0563	0.0001	0.986	525.3	5.1	464	4	–13

Note: Uncertainties are given at the 1σ level. Error in 44069 reference monazite calibration was 0.87% and 0.27% for the analytical sessions (not included in above errors but required when comparing $^{206}Pb/^{238}U$ data from different mounts). Common Pb made using the measured $^{204}Pb/^{206}Pb$ ratio.

†f_{206} % denotes the percentage of ^{206}Pb that is common Pb.

§For % disc, 0% denotes a concordant analysis.

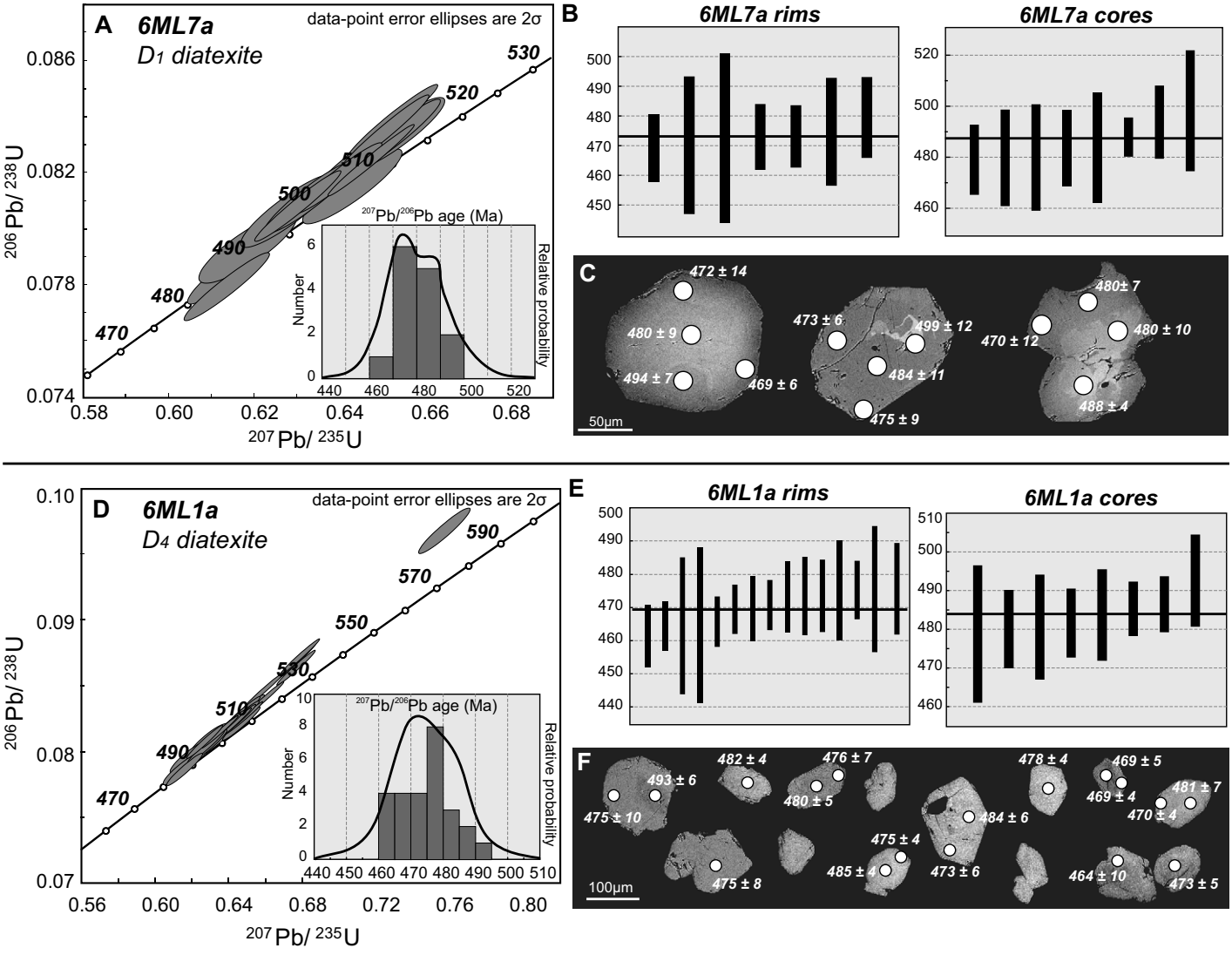

Figure 5. Results of monazite geochronology for diatexite sample 6ML7a related to early D_1 deformation (A–C) and for diatexite sample 6ML1a related to late D_4 deformation (D–F). (A) Wetherill concordia diagram for all analyses from sample 6ML7a. Error ellipses are 2σ. Inset shows $^{207}Pb/^{206}Pb$ ages (Ma) probability density plot for all individual data. (B) Weighted mean average plot of $^{207}Pb/^{206}Pb$ ages for monazite rims and cores in sample 6ML7a. Error bars are 2σ. (C) Backscattered electron (BSE) images of monazite grains from sample 6ML7a. Analyzed spots with single $^{207}Pb/^{206}Pb$ ages marked. Uncertainties are given at the 1σ level. (D) Wetherill concordia diagram for all analyses from sample 6ML1a. Error ellipses are 2σ. Inset shows $^{207}Pb/^{206}Pb$ ages (Ma) probability density plot for all individual data. (E) Weighted mean average plot of $^{207}Pb/^{206}Pb$ ages for monazite rims and cores in sample 6ML1a. Error bars are 2σ. (F) BSE images of monazite grains from sample 6ML1a. Analyzed spots with single $^{207}Pb/^{206}Pb$ ages marked. Uncertainties are given at the 1σ level.

leucosomes/sheets that converge toward antiformal hinge zones (Fig. 6A). Where this array of leucosomes is more intense, rock continuity in and around the hinge is disrupted, giving rise to a mobile diatexite sheet (Fig. 6A).

Layer-parallel leucosomes are linked continuously with long, narrow sheets of diatexite oriented at high angles to metatexite layering. Leucosomes on both sides of the high-angle sheet bend in the same direction (unidirectional bending), creating a cuspate and pierced fold hinge. Leucosomes form a funnel-shaped network converging toward a central channel (Fig. 6B). Diatexite sheets are roughly parallel to the axial-planar orientation of the folds and are commonly, but not always, found cutting across, breaking up, and transposing fold hinges, causing sharp truncations of metatexite layering (Fig. 6A).

An associated feature is the truncation of S_0 by sharp faults in the vicinity of hinge zones (Figs. 6C and 6D). These faults are asymmetric in that the block on one side of the fault is cut sharply by the fault, whereas the block on the other side is dragged, so that bedding planes, S_0, rotate into parallelism with the fault plane (Fig. 6C). Typically, the block that includes the hinge zone of the fold is truncated, whereas the block that contains the limb is dragged down. The fault plane is commonly, but not always, filled with enclave-rich diatexite, which is linked continuously with leucosomes (Figs. 6C and 6D). On subhorizontal outcrops, which are nearly perpendicular to the upright axial plane of the folds, the same faults can be recognized by the truncation of S_0 by a diatexite band on

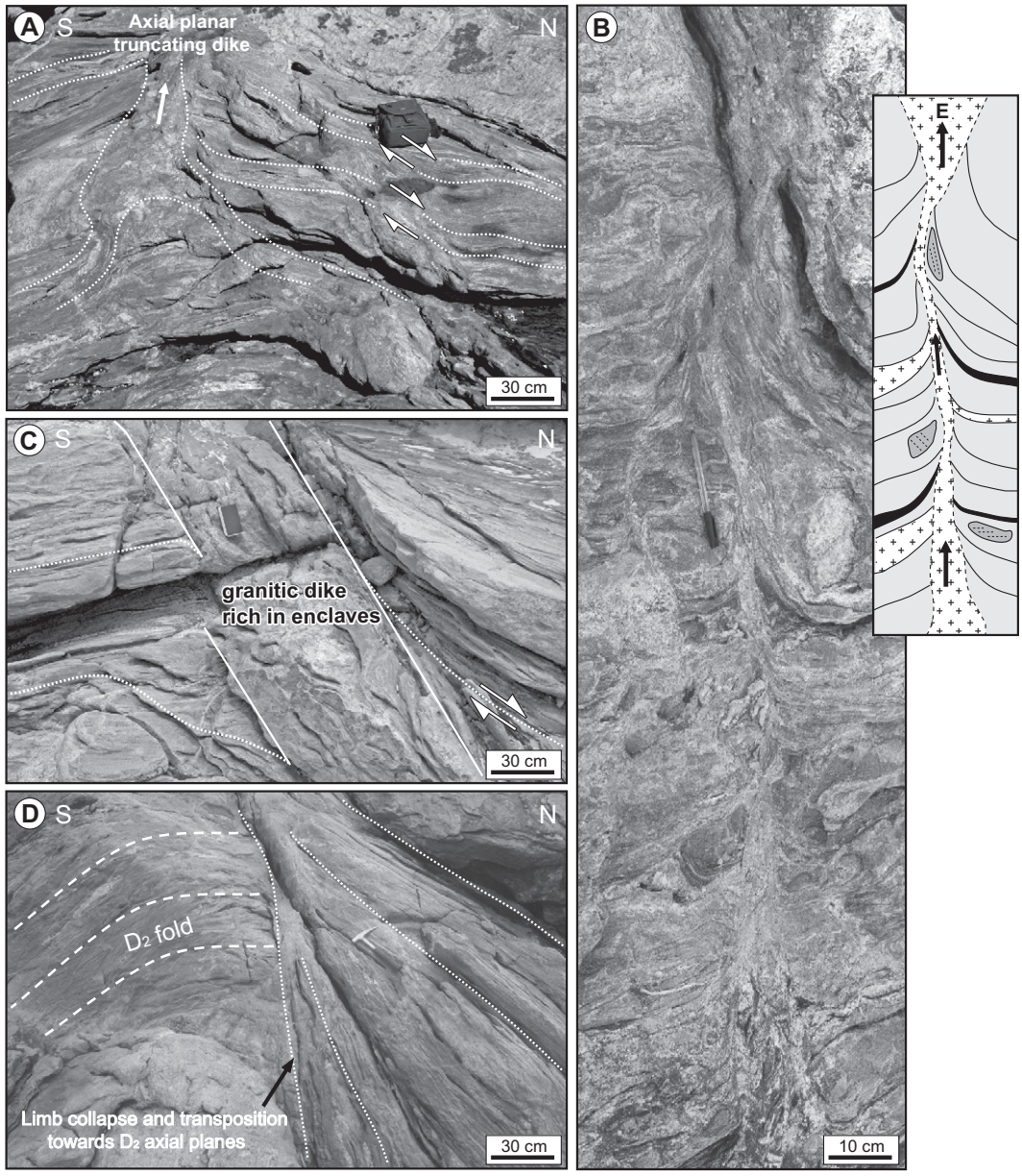

Figure 6. D_2 folding and axial-planar magma migration in Vivonne Bay area (Fig. 1). (A) Convergence of granitic dikes (white dashed lines) toward antiformal hinge zone. Individual dikes accommodate shearing, and fold hinge has been broken up by intrusions and lost layer continuity. Main trend of steeply dipping dikes at hinge zone is approximately E-W; foliation on north limb (right): 060°/28°N, on south limb (left): ~315°/20°SW. (B) Leucosomes merging eastward (up in figure) forming a funneling network trending approximately E-W and dipping steeply, crosscutting preexisting foliation at high angles (see inset). Network trend is subparallel to axial plane of upright folds and creates a band of diatexite within metatexite (locality VB2). (C–D) Looking west, down plunge of folds. (C) A 50-cm-wide granitic dike with metasedimentary enclaves in a fault truncating bedding on the left-hand side and dragging bedding into parallelism to the fault on the right-hand side. The fault is oriented approximately parallel to F_2 axial planes, and the deformation gives rise to N-S shortening, similar to the strain derived from upright D_2 folds. (D) Axial-planar fault truncating D_2 fold hinge, similar to C. On the north side, S_0 defines a drag fold indicative of north-limb-down shear sense. Fault lacks magma intrusion but has numerous layer parallel leucosomes.

one side of the fault and by conformity between the two on the other side (Fig. 7). In some cases, the sharp truncating fault planes are filled with irregular, amalgamated blocks of schollen, folded and stretched, separated by narrow leucogranitic heterogeneous rock (Fig. 7).

On a microscale, metatexites generally lack evidence of solid-state internal deformation. Only locally do quartz grains show incipient subgrain boundaries, locally defining a weak chessboard pattern (Fig. 8A), indicating high temperatures (>700 °C) within the stability field of high quartz (Kruhl, 1996). Leucosomes consist of Qtz + Pl + Kfs ± Bt ± Ms ± Tur ± Zrn ± Mnz (abbreviations after Kretz, 1983). Coarse-grained quartz, plagioclase, and K-feldspar in leucosomes preserve igneous textures with euhedral grain shapes and small interstitial quartz grains. Plagioclase is commonly found as strongly corroded inclusions in tartan-twinned K-feldspars (Fig. 8B). Quartz grain boundaries when facing feldspars are strongly curved, resulting in amoeboidal shapes (Gower and Simpson, 1992) with delicate and numerous embayments indicating corroded magmatic grain boundaries (Fig. 8C). Mesosomes consist of Qtz + Pl + Kfs ± Bt ± Ms and typically have polygonal "foam-like" texture indicating static recrystallization (Fig. 8D). Combined, these features indicate weak to negligible solid-state, postanatectic deformation (see Sawyer, 1998).

D_4 Dextral Shearing and Diatexite Deformation

This section describes a 300-m-long diatexite exposure along the Six Mile Lagoon coast (outcrop 6ML1). Diatexites here preserve structural features that demonstrate the nature of deformation and magma migration. This outcrop has numerous sigma-shaped schollen linked with

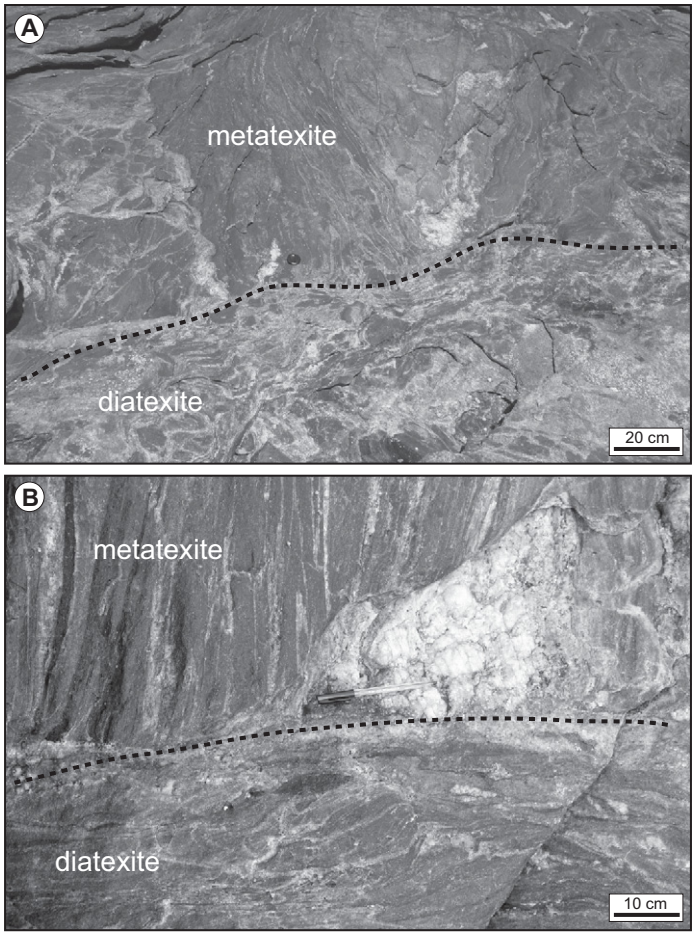

Figure 7. Truncation of metatexite by transposed band of diatexite oriented roughly E-W and steep, parallel to the axial plane. Leucosomes in diatexite are linked continuously with layer-parallel leucosomes in metatexite. The transposed zones have a well-defined, boundary-parallel foliation (black dashed line). (A) Note: schollen in diatexite form an irregular pattern. (B) Note: individual schollen cannot be defined and are separated either by thin leucosomes or by a diffuse band.

schlieren, which together define asymmetric patterns indicative of dextral shearing (Fig. 9). This interpreted shear sense is further supported by two orientations of the foliations in surrounding diatexites defined by schlieren and stretched schollen: a dominant and continuous foliation oriented ~075°/60°N and a less dominant foliation trending ~015°/70°W, which is dragged into the dominant one (Fig. 9A), defining an S-C pattern. Shear planes are spaced by approximately 1 m, which is also the typical length of the larger schollen (Fig. 9A).

Diatexite layers parallel to the dominant C plane are more granitic, with fewer and smaller schlieren and schollen, than diatexite layers aligned along the interpreted S planes in between schollen. The latter have a more intense schlieren foliation marked by more numerous and more elongated biotite pods and schlieren. This difference is interpreted as indicative of melt transfer from shortened S plane to C planes, as would result from deformation including a transtensional component of deformation. In detail, many leucosomes inside the schollen are continuous with the surrounding diatexite (Fig. 9B), indicative of contemporaneous presence of melt inside and outside the schollen. The interpreted synmagmatic dextral shear zones trending ~075° are further interpreted as being part of D_4. This is because of similarity in shear sense and orientation with smaller D_4 shear zones (see previous analysis and Figures 4C, 4D, and 9A), and because it lacks other overprinting deformation phases.

At microscale, similar to metatexites (Fig. 8), diatexites show only incipient to weak deformation. Leucosomes consist of Qtz + Pl + Kfs ± Bt ± Ms ± Tur ± Zrn ± Mnz and have typical igneous textures, such as euhedral plagioclase and interstitial, generally undeformed quartz grains. Most quartz grains lack a record of internal deformation, with only a few grains showing incipient undulose extinction. Incipient deformation is also indicated by K-feldspar grains, which have localized development of tartan twinning (e.g., Eggleton, 1979; Vernon, 2004). Mesosomes consist of Qtz + Pl + Kfs ± Bt ± Ms, and the felsic grains form a polygonal mosaic indicative of static recrystallization. Combined, these features suggest that flow probably took place in the partially melted state (see Sawyer, 1998).

Late- to Post-D_4 Magma Migration

This section focuses on diatexite-filled structures that crosscut the main D_4 shear-related structures, and therefore are interpreted to postdate this main dextral-normal movement (Fig. 10). These diatexite-filled structures are well displayed in exposures at Six Mile Lagoon (outcrop 6ML1). Beyond the sheared schollen described in the previous section (Fig. 9A), the most obvious feature of this outcrop is the presence of several, meter-long magmatic (diatexitic) sheets or irregular dikes that are directly linked with leucosomes in surrounding migmatites (Fig. 10). These sheets are heterogeneous, varying in composition from leucogranitic and leucotonalitic to heterogeneous, biotite-rich diatexites varying in grain size and proportion of schlieren and schollen (Figs. 10B–10D). They also have an internal foliation (Figs. 10B and 10C) that could have resulted from magmatic flow intensifying where a funnel narrows (Fig. 10B) or from to melt loss or in response to residual stresses. The magmatic sheets are reminiscent of the axial-planar diatexite sheets associated with D_2 folds described earlier herein (Fig. 6). They trend dominantly N-S, generally at a high angle to D_4 structures, and dip steeply (Fig. 10A). Their orientation is approximately parallel to the interpreted S planes related to dextral shearing during D_4 (Fig. 10A). Surrounding leucosomes are generally bent unidirectionally toward the central sheet in its immediate vicinity, forming a funnel-shaped structure with ill-defined margins (Figs. 10B and 10C). The central sheet may either be continuous with surrounding leucosomes or may truncate them, and this may vary along the sheet margins over tens of centimeters (Fig. 10C). Many magmatic sheets are internally complex, with irregular layering, disrupted and stretched rafts, and commonly have multiple meter-long schlieren (Fig. 10D). These schlieren are commonly, but not always,

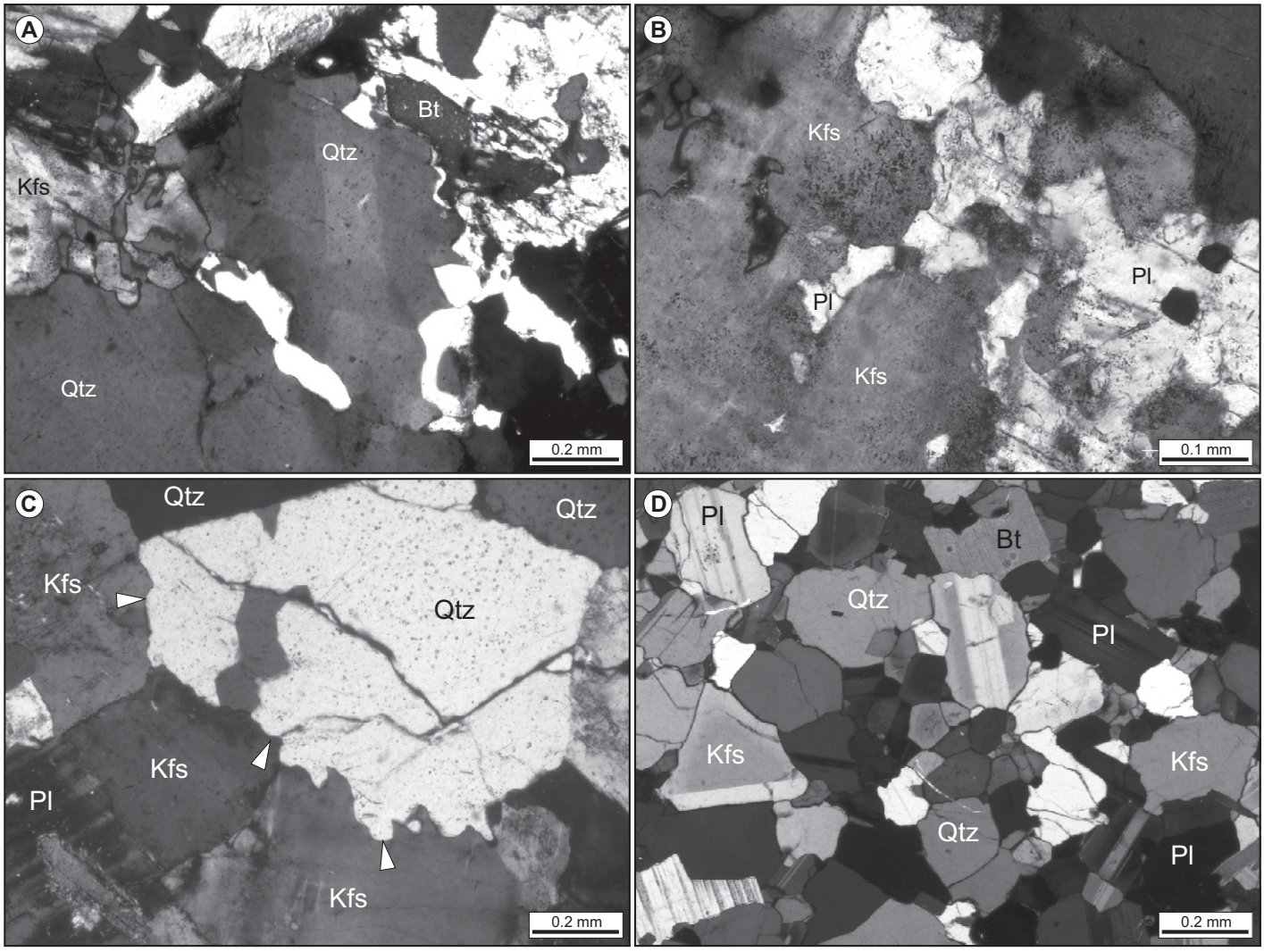

Figure 8. Photomicrographs (locality VB2 in Fig. 1) showing characteristic lack of solid-state deformation in metatexites and diatexites. (A) Weak chessboard pattern in quartz (sample VB2b). (B) Strongly corroded plagioclase grain in tartan-twinned K-feldspars (sample VB2b). (C) Strongly curved, amoeboidal quartz shapes when facing feldspars (white arrows; sample VB2c). (D) Polygonal "foam-like" mosaic of plagioclase (Pl), K-feldspar (Kfs), and quartz (Qtz) in mesosome (sample VB2a). Bt—biotite.

developed at sheet margins, and occasionally a single schlieren bifurcates around a solid inclusion or a schollen (Fig. 10D). In some places, larger schollen trending parallel to the dominant shear foliation (ENE-WSW) are bounded on either side by these N-S–trending sheets (Figs. 10C and 11A). Leucosomes in the schollen can be linked directly to leucogranite in the sheets, and both sides of the schollen are bent to the north (unidirectional bending), leading to a broad U shape (Fig. 11). This is indicative of the continued presence of melt from D_4 shearing to post-D_4 magma extraction.

These irregular, heterogeneous sheets may also be linked with metric equidimensional bodies of leucogranite with ill-defined margins against diatexite. In one case the irregular leucogranite body contains equidimensional biotite-rich schollen <10 cm in diameter, and it links with a funnel-shaped region, narrowing to the north, in which schollen become increasingly elongated defining a N-S foliation parallel to the funnel walls. Further to the east (outcrop 6ML2; 36°01′16.2″S, 137°03′24.3″E), the diatexite grades into an enclave-rich granite with schlieren similar to those in the diatexite (Fig. 12). Unlike the diatexite, the dominant fabric in the granite is roughly N-S, marked by the orientation of meter-scale schlieren and oriented migmatitic enclaves (Fig. 12). This suggests transposition of the fabric of the migmatitic protolith within these magmatic bodies.

Like D_4, these late features developed in the presence of magma in the diatexite, but they are either late-D_4 or postdate the fabric developed during D_4, lacking clear evidence of being associated with an externally driven deformation event (Fig. 10). Leucosomes and melanosomes are dragged into N-S–trending sheets funneling to the north, at high angle to the dominant D_4 shear plane (Figs. 10 and 11A). These sheets are interpreted as magma channels or dikes that tapped a mobile diatexite and drained them toward the north (Fig. 10A).

DISCUSSION

Migmatites on Kangaroo Island reveal complex structural patterns as a result of magma migration and multiple deformation events. This section starts with a discussion of the

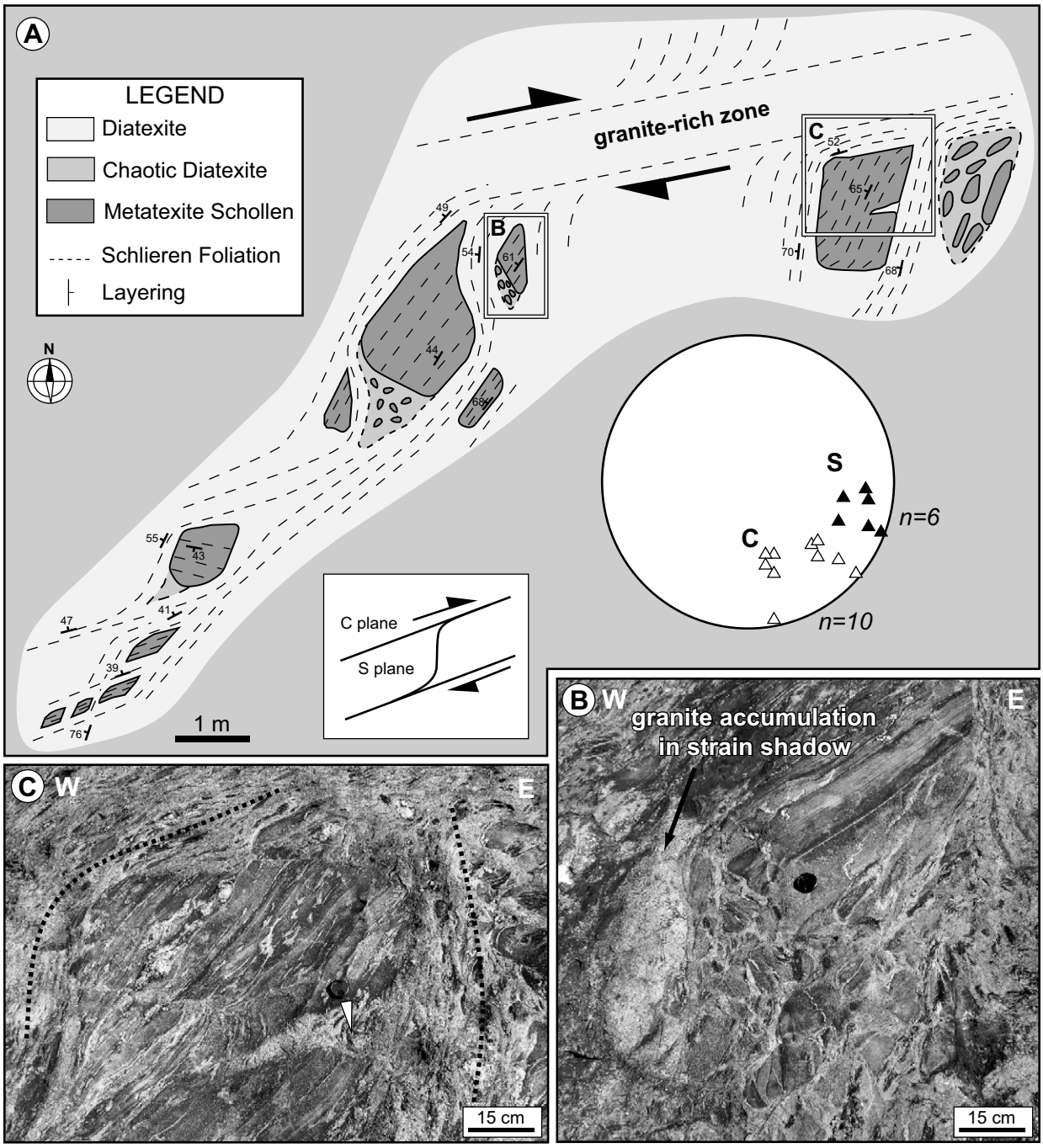

Figure 9. D_4 shearing and diatexite deformation. (A) Detailed geologic map of sheared diatexite (locality 6ML1). Dextral shearing in the plane of exposure (close to horizontal) is inferred from the two dominant foliations defined by the asymmetric shape of schollen, orientation of schlieren, and distribution of magma-rich bands. Individual schollen have sigmoidal shapes wrapped by foliation in surrounding diatexite, well defined by schlieren and elongated and disrupted schollen. Insets show schematically the shear plane, C, trending ~N60°–70°E, dipping moderately to steeply NW. These planes drag an S foliation, striking NNE, and defining a dextral shear sense. Black rectangles mark the position of photographs in B and C. Stereonet shows poles to C and S planes (equal-area, lower-hemisphere projection). Number of measurements is indicated (*n*). (B) Breakup of asymmetric, sigmoidal schollen. Its west side has been broken up into small and rotated blocks in a granitic matrix (notice difference in foliation orientation in amongst blocks). Asymmetric shape of the main schollen and its disrupted parts is indicative of dextral shearing. Notice granite accumulation on inferred strain shadow. (C) Schollen in diatexite with external foliation wrapping around margins (black dashed line). Internal, gray leucosomes are continuously linked to the external diatexite and record the process of schollen breakup (e.g., just below the lens cap, white arrow).

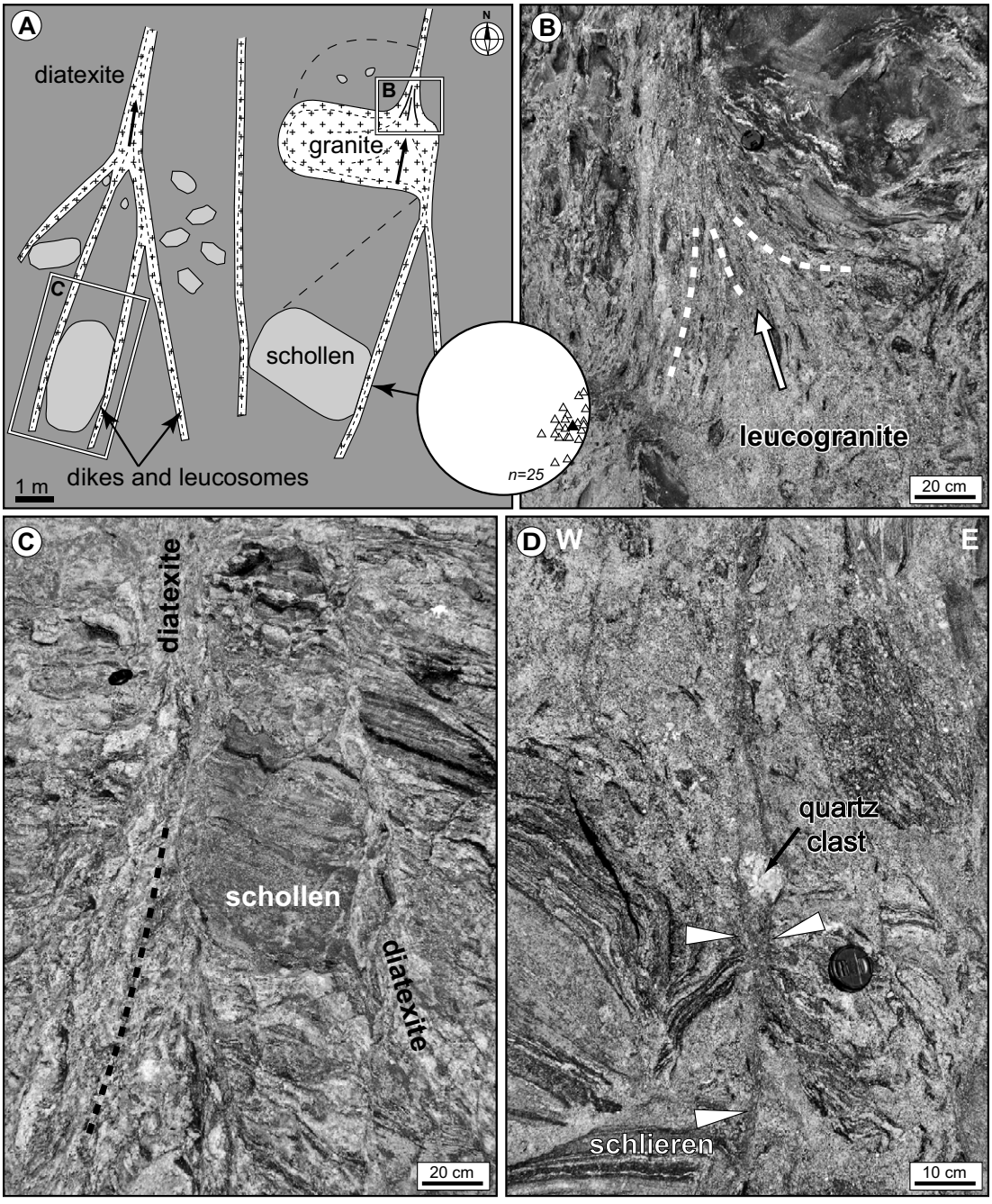

Figure 10. Characteristic features of late- to postkinematic magma migration. (A) Geologic map of part of the Six Mile Lagoon outcrop, only a few meters from map in Figure 9, showing distribution of long, leucocratic sheets in diatexite including meter-scale schollen of source rock. Locations of photographs in B and C are indicated. Stereonet shows poles to the magmatic sheets/dikes orientation (white triangles; equal-area, lower-hemisphere projection). Black triangle indicates average value of poles to S planes related to dextral shearing during D_4. Number of measurements is indicated (*n*). Dashed black lines indicate foliation. (B) A northward-funneling structure (white dashed lines) in which small schollen are increasingly elongated. This structure is linked to a meter-scale region of clean leucogranite with a few equidimensional schollen, which is itself linked to other leucocratic sheets. See A for sketch of relationships. (C) N-S–trending sheets of diatexite separating regions trending approximately E-W preserving large schollen and an earlier migmatitic layering. These sheets show visible internal foliation (black dashed line). The sheets widen and split into a network of smaller leucosome sheets toward the south (lower part of photograph). Leucosomes in surrounding migmatite bend into and are continuous with the N-S diatexite sheets. (D) Long, N-S–trending schliere splits into two (white arrows) and wraps around a quartz clast (black arrow), suggesting sheet closure by magma expulsion, except for the region protected by the quartz clast.

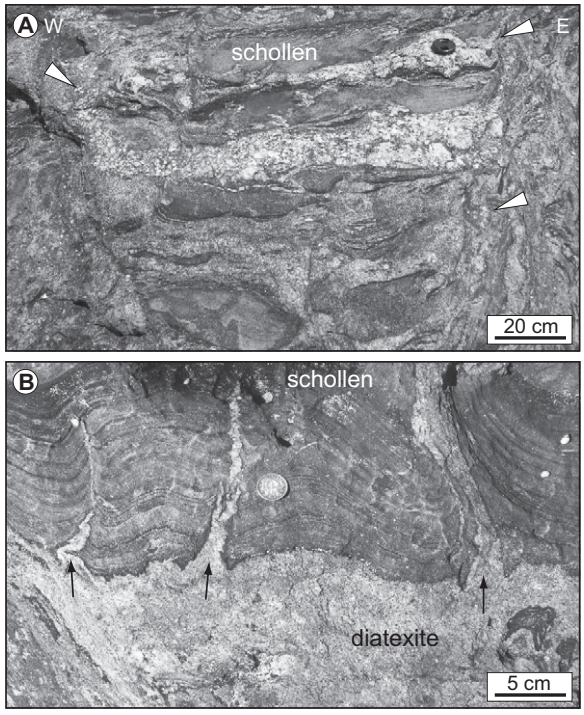

Figure 11. Characteristic schollen appearance. (A) U-shaped schollen with internal layering trending E-W and dragged northward at the margins (white arrows). (B) Schollen within a diatexite with granitic dikelets intruding upward-bending (unidirectional) drag folds, suggestive of forceful intrusion of the magma.

timing of anatexis and is followed by a discussion of the evolution of deformation and influence on magma extraction and migration. We suggest contrasting behavior during early folding, when antiform hinges served as natural focusing paths for magmas, and during later oblique normal-dextral shearing, when dilational deformation led preferentially to magma accumulation rather than migration. As deformation was waning, magma was further extracted from leucosomes into channels by either magma buoyancy or residual pressure differences at large scale. These late- to postkinematic magma migration structures are comparable to structures that develop during dewatering in soft sediments.

Figure 12. Diatexites grade into regions that consist of a more homogeneous granitic groundmass and fewer and better-defined individualized schollen or enclaves. Close to the diatexite of Six Mile Lagoon, granitic outcrops such as this have numerous long biotite-muscovite schlieren oriented approximately N-S, parallel to enclave length, unlike diatexite outcrops where schollen were oriented at high angles to dikes and schlieren. North is to the righ of the photograph.

Duration of Anatexis

Timing of anatexis on Kangaroo Island was studied by Tassone (2008), who dated monazites (U-Pb LA-ICP-MS) in leucosomes and mesosomes in migmatites in Vivonne Bay, Six Mile Lagoon, and Stun Sail Boom (Fig. 1). Tassone (2008) obtained ages between ca. 498 Ma and 488 Ma (considering the spread of average ages of all samples; single age distribution spreads between 557 Ma and 411 Ma), with mean weighted average of 493.6 ± 4.0 Ma, and interpreted these ages as crystallization ages. This implies that partial melting occurred late, just prior to the cessation of the Delamerian orogeny (Foden et al., 2006). Tassone's (2008) ages have a significant age spread (>10 m.y.), but no satisfactory explanation for the age spread is provided.

Our monazite geochronology data show for each sample a continuous age spread between ca. 495 Ma and 465 Ma (Fig. 5; Table 1), which matches the age range described by Tassone (2008). However, our ages seem to be slightly younger, which might be a result of our choice of using the more reliable $^{207}Pb/^{206}Pb$ ages for these reversely discordant and very U-rich monazites (e.g., Stern and Berman, 2000; White and Ireland, 2012). Although Tassone (2008) discussed concordant LA-ICP-MS monazite $^{238}U/^{206}Pb$ ages, he did not present U or Th concentrations for his monazites. Therefore, it is difficult to make further comparisons.

The spread of ages in our two samples is a common feature in high-grade rocks, especially those that have undergone a partial melting event (Foster et al., 2002, 2004). Foster et al. (2002) concluded that the age dispersal in high-grade rocks results either from growth/recrystallization of monazite during a single metamorphic event or discontinuous growth during several events. Like Foster et al., we consider the continuous age spread to indicate the broad duration of the partial melting event, which therefore lasted between ca. 495 Ma and ca. 465 Ma.

Both our samples show zoned monazites with a similar range of core ages (ca. 495–480 Ma; Figs. 5B and 5E) and rim ages (ca. 480–465 Ma; Figs. 5B and 5E). Although these two age groups overlap, they are distinguished based on textural observations (cores and rims of monazites). When magma starts to crystallize, monazite grains begin to nucleate. These monazites grow while new monazites nucleate as the magma cools. This results in zoned monazites reflecting grain growth, and also in homogeneous, nonzoned monazites that were either reset or nucleated last, as observed in our samples (Fig. 5). Monazites in both our samples have a similar grain size range, 50–150 μm,

clear euhedral to rounded shapes, and no signs of recrystallization or corrosion (Figs. 5C and 5F), suggestive of a simple crystallization and growth.

Different sections of the outcropping migmatites reached maximum melt fraction at different times, as indicated by the dominant syn-magmatic structures recorded. This means that while a particular section may still have had significant melt volumes, others may have solidified. Kelsey et al. (2008) showed that most monazite growth occurs close to the solidus, where low-volume melts crystallize over a narrow range of temperatures. This would imply that either monazite grains grew at different times in different outcrops, or that the system as a whole stayed close to the solidus for a considerable time and recorded the same age range. The latter seems to be the option supported by the data.

In the regional context of rising and falling temperatures, leading to peak anatectic conditions, the age ranges determined mark the beginning and end of monazite growth. These ages overlap broadly, but not necessarily precisely, with the anatectic period. Thus, taken together, the monazite ages indicate that anatexis may have lasted over 30 m.y. The older ages mark the onset of monazite growth and the younger monazite grains grew close to the regional solidus. An alternative interpretation is that radiogenic Pb-loss led to an apparent dispersion in ages during the youngest event pulling the older ages towards the younger ones. In this case, there may have been two distinct melting events.

Magma Channeling during Folding: Hinge Disruption and Transposition, Limb Collapse

The features depicted in Figure 6 are interpreted as recording a magma escape network that developed contemporaneously with folding. Fold initiation created pressure gradients that focused magma migration toward incipient antiforms and caused volume loss at fold limbs. The process led to fold amplification and disaggregation of magma-rich fold hinge zones, to form diatexites that gradually became interconnected, allowing magma escape, limb collapse, and rotation of blocks (Fig. 6). The funneling direction of the leucosome network is interpreted as indicating the direction of magma flow (Fig. 6B), and the network itself is interpreted to represent the root zones of axial-planar diatexitic or granitic dikes (see cusp folds in Weinberg and Mark, 2008). The cases where the central channel is composed of amalgamated blocks of source rock are interpreted as the remainders of a diatexite where the interstitial mobile magma escaped, leaving behind a schollen aggregate.

The process of magma migration during folding described here was inferred from relatively small features. However, it is plausible that the same processes lead to larger-scale features. For example, the process could explain common meter-scale examples of truncation of metatexites along axial-planar orientations by diatexite bands or "dirty" granites (Fig. 13).

Folding and magma migration can also lead to complex features. Figure 14A depicts complex relationships among magma migration, folding, shearing, and boudins, exemplifying the difficulties in interpreting migmatite terranes. The figure can be interpreted as a root zone of a magma channel fed from both a cuspate fold hinge zone and from a shear band, linked continuously with layer-parallel leucosomes (lower right). The main channel (emphasized by black dashed line) seems to be crossing through a boudin neck. The complexities depicted are interpreted as representing the local history of heterogeneous magma extraction and structural development.

In summary, magma extraction from folded metatexites occurs through magmatic dikes developed in the hinge zones of antiforms. They result from the funneling of a network of leucosomes toward the hinge zones (Figs. 6B and 14B). Magma migration drags the metatexite, forming cusp-shaped fold hinges, or shear zones, and disaggregates the solid mass to form schollen-rich diatexites. Melt-lubricated faults allow for magma extraction and limb collapse (Fig. 14B). This process is responsible for transposed axial-planar regions of amalgamated blocks of source rock (schollen) left behind after magma is extracted (Figs. 6B and 11A).

Shearing of Diatexites and Schollen

The diatexites from Six Mile Lagoon preserve only locally coherent structures related to D_4. Considerable sections of the outcrop lack coherence, suggesting that at least part of D_4 structures may have been destroyed by stress

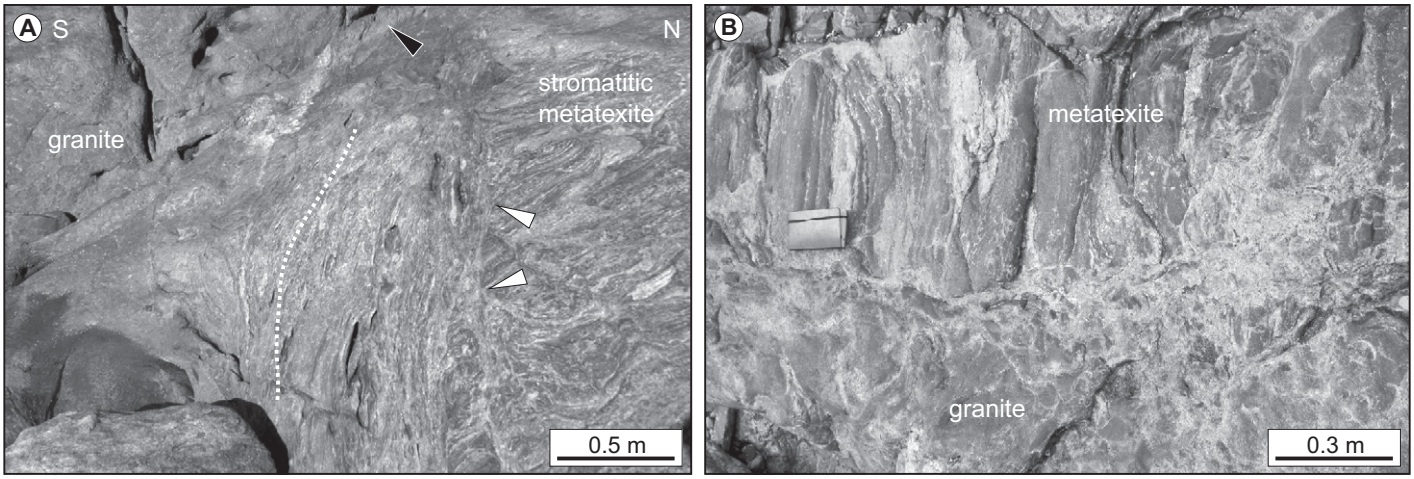

Figure 13. (A) Contact at locality VB2 between a several-meter-wide granite sheet and stromatic metatexite separated by a zone of transposed and disrupted migmatite with intense foliation, which truncates the metatexite (white arrows). The disrupted migmatite has a strong internal foliation (white dashed line) characterized by stretched schollen. The truncation plane strikes approximately E-W and dips 85°N, parallel to F_2 axial planes, and is parallel to the foliation in the transposed zone. Contact between granite and transposed zone is locally irregular, and eastward, granite cuts across transposition zone (black arrow). (B) Truncation of metatexite by a gray granite with leucocratic (white) veins, forming a network that crosses the boundary between the two rock types (at Point Ellen).

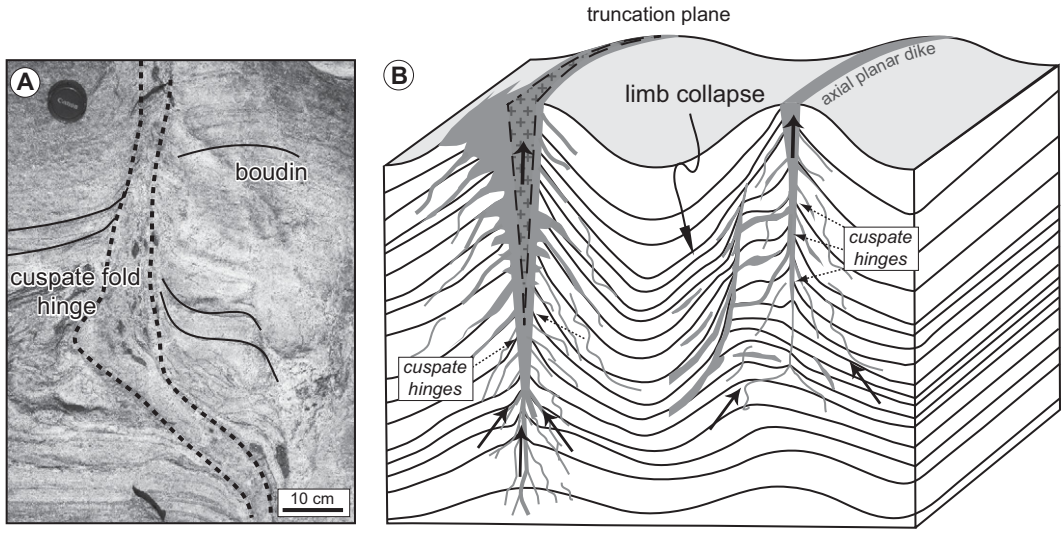

Figure 14. (A) Photograph depicts complex interaction among folding, shearing, boudinage, and magma flow in metatexites. Gently folded metatexite is cut across by magma sheets (black dashed lines) with disrupted solid rafts and schlieren defining shear zones. The pattern can be interpreted in terms of magma escape through limbs and hinge zones of a gently folded sequence. Magma pathways are oriented parallel to the axial plane of folds, and magma extraction from the surrounding rocks leads to structural complexity such as layer-parallel boudinage. (B) Schematic summary of noncylindrical antiforms channeling magma out of metatexites during D_2, giving rise to axial-planar dikes and limb collapse. Dikes may be granitic with few schollen, or they may be made up of stretched-out schollen with a small volume of leucosomes separating them. They may be linked continuously with leucosomes in metatexite, and metatexite may be dragged to form cuspate hinges (dashed arrows), or they may truncate layering. Limb collapse results from the process of magma loss, activation of a melt-lubricated fault, and magma transfer along the fault plane, truncating the hinge zone on one side and dragging the limb downward on the other side.

relaxation while the diatexites were still partially molten. This relaxation is evidenced by the late- to post-D_4 magma extraction features (Fig. 10) that may have been accompanied by minor but generalized flow of the diatexite and schollen rotation.

Typically, a fluid is unable to impart significant shear stress to a solid. However, features such as those shown in Figure 13 are common and show how intrusive granite dikelets are capable of dragging layers in the surrounding schollen. More generally, the fact that schollen were sheared within a partially molten diatexite during D_4 indicates low viscosity contrasts between the two. This may have been a result of the presence of a significant melt fraction in the schollen (>7%; Rosenberg and Handy, 2005) and the presence of a significant amount of solids in the diatexite.

Late- to Postkinematic Magma Drainage

The N-S–trending dikes documented at Six Mile Lagoon postdate D_4 dextral-normal shearing (Fig. 10). This is evidenced by the bending, transposition, and truncation of the dominant D_4 shear planes, originally oriented at a high angle to the dikes. These dikes are interpreted as late- to postkinematic because they are not obviously associated with any independent, forced deformation of the rock mass. Deformation at this stage was directly associated with the dikes and can be ascribed to magma flow itself, such as the unidirectional dragging of foliation at the margin of dikes, and stretching and disaggregation of rafts within and parallel to the dike orientation (Fig. 10). Magma migration requires a pressure gradient, which could be from residual regional stress differences from the waning deformation, or magma buoyancy.

Like the magma channels associated with folds, the dikes and associated structures are interpreted as representing magma extraction networks, where each dike represents a pathway fed by leucosomes or mobile diatexite in the surrounding mass, converging and migrating northward at multiple scales. This interpretation is based on the trend of the magma sheets combined with unidirectional features, such as leucosome networks funneling northward, and the dragging of preexisting layering to the north, features that are interpreted to mark dike roots (Fig. 10). North-directed migration was inferred based on two-dimensional indicators (see also Weinberg and Mark, 2008) on dominantly horizontal planes and represents a projection onto the outcrop of the true flow vector. This N-directed flow gave rise to the long schlieren, commonly at dike margins, and the splitting of the schliere in Figure 10D around the quartz clast is interpreted to record the squeezing out of most of the magma in a channel, impeded locally by the presence of the clast. The metric pocket of leucogranite within the diatexite in Figure 10A is interpreted to mark a magma pool from which some mobile magma was extracted northward by the funnel-shaped root. This magma flow caused stretching and shearing of the equidimensional schollen.

Sediment Dewatering Structures: An Analogue to Late- to Postkinematic Magma Extraction

The late- to postkinematic features of magma extraction have a number of features in common with dewatering structures in sediments (Fig. 15). The comparison is warranted by the physical similarity between the systems: both represent remobilization of a solid by movement of interstitial fluid responding to pressure gradients. A fundamental difference between the two is that any melt remaining in the system is eventually solidified to form granitic rocks.

Like the interpreted magma drainage features, sediment dewatering channels form at high angle to bedding, break up, and transpose bedding by dragging, rotating, and deforming sand layers (Figs. 10 and 15). Sand blocks form coherent but folded blocks and may also be broken down to schlieren, leading to partial homogenization of the matrix by the mixing of sand grains with mud. Flow channels merge and narrow upward, forming a funnel-shaped root zone (Fig. 15).

We suggest that the larger-scale features recorded in the migmatites at Six Mile Lagoon are essentially similar to those recorded by sediment dewatering, where a liquid escapes

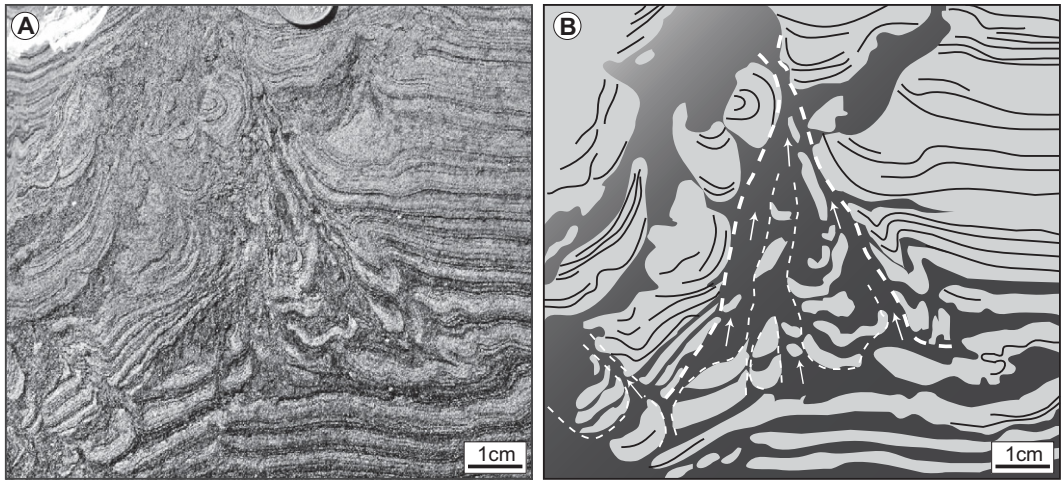

Figure 15. (A) Photograph and (B) sketch of dewatering structures in soft sediments analogous to those in migmatites. This block is from an upper-greenschist-facies, Kanmantoo Group layered sandstone-mudstone sequence from Harvey's Return, on the north side of Kangaroo Island. Mud layers were fluidized and escaped through a network of converging channels forming a funnel-shaped path, narrowing upward (white dashed lines). Flow dragged, broke up, and deformed sand layers (in gray). Individual sand blocks have both margins dragged upward (U-shaped) and are sometimes linked to upward-pointing cuspate folds. The matrix mudstone (black) gradually becomes gray toward the upper-left corner of the photograph due to mixing with disrupted sand grains.

the interstices between solids and liquefies the system, breaking up more coherent masses into rafts and giving rise to an interlinked funnel-shaped network of channels that drain magma (Figs. 10 and 15). The different length scales relate directly to grain size, the strength of coherent layers, liquid viscosity, and differences in pressure gradients. Magmatic systems typically have large grain size, and higher liquid viscosity, therefore requiring larger-scale flows and channel widths for magma to escape efficiently and disaggregate the original rock. The similarity in raft behavior suggests that the ratio between flow drag acting on the blocks and block coherence is similar in the two systems.

In summary, during folding, the hinges of anticlines acted as natural funneling paths for magmas, providing the starting points for dikes (Fig. 6). In contrast, during transtensional shearing, diatexites formed, possibly because deformation was conducive to magma accumulation rather than escape (Fig. 9). Finally, in the absence of a strong stress field as transtensional deformation was waning, melt self-organized into magma extraction channels rooted in funneling leucosomes, driven either by residual pressure differences at large scale and related to previous deformation, or driven by magma buoyancy (Fig. 10). Structures that formed in the magma source in this case are similar to those related to sediment dewatering (Fig. 15).

ACKNOWLEDGMENTS

This work was financially supported by the Australian Research Council grant DP110102543. P. Hasalová acknowledges funding from the Ministry of Education of the Czech Republic (grant LK11202). We would like to thank Bin Fu from the Australian National University for assistance with the geochronology sample preparation and monazite backscattered-electron imaging. We also thank Mike Brown and an anonymous reviewer for their constructive reviews, which much improved the manuscript, and the *GSA Bulletin* Editor Christian Koeberl and Associate Editor Roger Gibson for all their editorial work on the manuscript.

REFERENCES CITED

Aleinikoff, J.N., Schenck, W.S., Plank, M.O., Srogi, L., Fanning, C.M., Kamo, S.L., and Bosbyshell, H., 2006, Deciphering igneous and metamorphic events in high-grade rocks of the Wilmington Complex, Delaware: Morphology, cathodoluminescence and backscattered electron zoning, and SHRIMP U-Pb geochronology of zircon and monazite: Geological Society of America Bulletin, v. 118, p. 39–64, doi:10.1130/B25659.1.

Belperio, A.P., and Flint, R.B., 1993, The southeastern margin of the Gawler craton: Australian Journal of Earth Sciences, v. 40, p. 423–426, doi:10.1080/08120099308728093.

Belperio, A.P., Preiss, W.V., Fairclough, M.C., Gatehouse, C.G., Gum, J., Hough, J., and Burtt, A., 1998, Tectonic and metallogenic framework of the Cambrian Stansbury Basin–Kanmantoo Trough, South Australia: AGSO Journal of Australian Geology & Geophysics, v. 17, p. 183–200.

Brown, M., 1973, The definition of metatexis, diatexis and migmatite: Proceedings of the Geologists' Association, v. 84, p. 371–382.

Brown, M., and Rushmer, T., 1997, The role of deformation in the movement of granitic melt: Views from the laboratory and the field, *in* Holness, M.B., ed., Deformation-Enhanced Fluid Transport: Mineralogical Society Book Series: London, Chapman and Hall, p. 111–144.

Brown, M., and Solar, G.S., 1998a, Granite ascent and emplacement during contractional deformation in convergent orogens: Journal of Structural Geology, v. 20, no. 9–10, p. 1365–1393, doi:10.1016/S0191-8141(98)00074-1.

Brown, M., and Solar, G.S., 1998b, Shear-zone systems and melts: Feedback relations and self-organization in orogenic belts: Journal of Structural Geology, v. 20, no. 2–3, p. 211–227, doi:10.1016/S0191-8141(97)00068-0.

Brown, M., and Solar, G.S., 1999, The mechanism of ascent and emplacement of granite magma during transpression: A syntectonic granite paradigm: Tectonophysics, v. 312, p. 1–33, doi:10.1016/S0040-1951(99)00169-9.

Brown, M., Averkin, Y.A., McLellan, E.L., and Sawyer, E.W., 1995, Melt segregation in migmatites: Journal of Geophysical Research, v. 100, no. B8, p. 15,655–15,679, doi:10.1029/95JB00517.

Clemens, J.D., and Mawer, C.K., 1992, Granitic magma transport by fracture propagation: Tectonophysics, v. 204, p. 339–360, doi:10.1016/0040-1951(92)90316-X.

Collins, W.J., and Sawyer, E.W., 1996, Pervasive granitoid magma transfer through the lower-middle crust during non-coaxial compressional deformation: Journal of Metamorphic Geology, v. 14, p. 565–579, doi:10.1046/j.1525-1314.1996.00442.x.

Cooper, J.A., Jenkins, R.J.F., Compston, W., and Williams, I.S., 1992, Ion-probe zircon dating of a mid Early Cambrian tuff in South Australia: Journal of the Geological Society of London, v. 149, p. 185–192, doi:10.1144/gsjgs.149.2.0185.

Cruden, A.R., 1988, Deformation around a rising diapir modeled by creeping flow past a sphere: Tectonics, v. 7, p. 1091–1101, doi:10.1029/TC007i005p01091.

Davidson, C., Schmid, S.M., and Hollister, L.S., 1994, Role of melt during deformation in the deep crust: Terra Nova, v. 6, p. 133–142, doi:10.1111/j.1365-3121.1994.tb00646.x.

Dymoke, P., and Sandiford, M., 1992, Phase relationships in Buchan facies series pelitic assemblages: Calculations with application to andalusite-staurolite paragenesis in the Mount Lofty Ranges, South Australia: Contributions to Mineralogy and Petrology, v. 110, no. 1, p. 121–132, doi:10.1007/BF00310886.

Eggleton, R.A., 1979, The ordering path for igneous K-feldspar megacrysts: The American Mineralogist, v. 64, p. 906–911.

Fanning, C. M., 1990, Single Grain Dating of a Granite Sample from Cape Willoughby, Kangaroo Island, Prise Laboratories, Australian National University, Progress Report 89–060: South Australia, Department of Mines and Energy Open-File Envelope 8828, p. 29–32.

Fleming, P.D., and White, A.J.R., 1984, Relationships between deformation and partial melting in the Palmer migmatites, South Australia: Australian Journal of Earth Sciences, v. 31, no. 4, p. 351–360, doi:10.1080/08120098408729297.

Flint, D.J., and Grady, A.E., 1979, Structural geology of Kanmantoo Group metasediments between West Bay and Breakneck River, Kangaroo Island: Transactions of the Royal Society of South Australia, v. 103, p. 45–56.

Flöttmann, T., and Cockshell, C.D., 1996, Palaeozoic basins of southern South Australia: New insights into their structural history from regional seismic data: Australian Journal of Earth Sciences, v. 43, p. 45–55, doi:10.1080/08120099608728234.

Flöttmann, T., Haines, P.W., Cockshell, C.D., and Preiss, W.V., 1998, Reassessment of the seismic stratigraphy of the early Palaeozoic Stansbury Basin, Gulf St. Vincent,

South Australia: Australian Journal of Earth Sciences, v. 45, p. 547–557, doi:10.1080/08120099808728411.

Foden, J., Sandiford, M., Dougherty-Page, J., and Williams, I., 1999, Geochemistry and geochronology of the Rathjen Gneiss: Implications for the early tectonic evolution of the Delamerian orogen: Australian Journal of Earth Sciences, v. 46, no. 3, p. 377–389, doi:10.1046/j.1440-0952.1999.00712.x.

Foden, J., Elburg, M.A., Turner, S.P., Sandiford, M., O'Callaghan, J., and Mitchell, S., 2002, Granite production in the Delamerian orogen, South Australia: Journal of the Geological Society of London, v. 159, p. 557–575, doi:10.1144/0016-764901-099.

Foden, J., Elburg, M.A., Dougherty-Page, J., and Burtt, A., 2006, The timing and duration of the Delamerian orogeny: Correlation with the Ross orogen and implications for Gondwana assembly: The Journal of Geology, v. 114, no. 2, p. 189–210, doi:10.1086/499570.

Foster, G.L., Gibson, H.D., Parrish, R.R., Horstwood, M.S.A., Fraser, J., and Tindle, A., 2002, Textural, chemical and isotopic insights into the nature and behaviour of metamorphic monazite: Chemical Geology, v. 191, p. 183–207, doi:10.1016/S0009-2541(02)00156-0.

Foster, G.L., Parrish, R.R., Horstwood, M.S.A., Chenery, S., Pyle, J., and Gibson, H.D., 2004, The generation of prograde *P-T-t* points and paths; a textural, compositional and chronological study of metamorphic monazite: Earth and Planetary Science Letters, v. 228, p. 125–142, doi:10.1016/j.epsl.2004.09.024.

Gower, R.J.W., and Simpson, C., 1992, Phase boundary mobility in naturally deformed, high-grade quartzofeldspathic rocks: Evidence for diffusion creep: Journal of Structural Geology, v. 14, p. 301–3134, doi:10.1016/0191-8141(92)90088-E.

Haines, P.W., Jago, J.B., and Gum, J.C., 2001, Turbidite deposition in the Cambrian Kanmantoo Group, South Australia: Australian Journal of Earth Sciences, v. 48, no. 3, p. 465–478, doi:10.1046/j.1440-0952.2001.00872.x.

Hawkins, D.P., and Bowring, S.A., 1997, U-Pb systematic of monazite and xenotime: Case studies from the Paleoproterozoic of the Grand Canyon, Arizona: Contributions to Mineralogy and Petrology, v. 127, p. 87–103, doi:10.1007/s004100050267.

Hollister, L.S., and Crawford, M.L., 1986, Melt-enhanced deformation: A major tectonic process: Geology, v. 14, p. 558–561, doi:10.1130/0091-7613(1986)14<558:MDAMTP>2.0.CO;2.

Ireland, T.R., Flottmann, T., Fanning, C.M., Gibson, G.M., and Preiss, W.V., 1998, Development of the early Paleozoic Pacific margin of Gondwana from detrital-zircon ages across the Delamerian orogen: Geology, v. 26, no. 3, p. 243–246, doi:10.1130/0091-7613(1998)026<0243:DOTEPP>2.3.CO;2.

Jago, J.B., Gum, J.C., Burtt, A.C., and Haines, P.W., 2003, Stratigraphy of the Kanmantoo Group: A critical element of the Adelaide fold belt and the palaeo-Pacific plate margin, eastern Gondwana: Australian Journal of Earth Sciences, v. 50, no. 3, p. 343–363, doi:10.1046/j.1440-0952.2003.00997.x.

Jenkins, R.J.F., and Sandiford, M., 1992, Observations on the tectonic evolution of the southern Adelaide fold belt: Tectonophysics, v. 214, no. 1–4, p. 27–36, doi:10.1016/0040-1951(92)90188-C.

Kelsey, D.E., Clark, C.F.P., and Hand, M.P., 2008, Thermobarometric modelling of zircon and monazite growth in melt-bearing systems: Examples using model metapelitic and metapsammitic granulites: Journal of Metamorphic Geology, v. 26, p. 199–212, doi:10.1111/j.1525-1314.2007.00757.x.

Kretz, R., 1983, Symbols for rock-forming minerals: The American Mineralogist, v. 68, p. 277–279.

Kruckenberg, S.C., Ferré, E.C., Teyssier, C., Vanderhaeghe, O., Whitney, D.L., Seaton, N.C.A., and Skord, J.A., 2010, Viscoplastic flow in migmatites deduced from fabric anisotropy: An example from the Naxos dome, Greece: Journal of Geophysical Research, v. 115, B09401, doi:10.1029/2009JB007012.

Kruckenberg, S.C., Vanderhaeghe, O., Ferré, E.C., Teyssier, C., and Whitney, D.L., 2011, Flow of partially molten crust and the internal dynamics of a migmatite dome, Naxos, Greece: Tectonics, v. 30, TC3001, doi:10.1029/2010TC002751.

Kruhl, J., 1996, Prism- and basis-parallel subgrain boundaries in quartz: A micro-structural geothermobarometer: Journal of Metamorphic Geology, v. 14, p. 581–589, doi:10.1046/j.1525-1314.1996.00413.x.

Lister, J.R., and Kerr, R.C., 1991, Fluid-mechanical models of crack propagation and their application to magma transport in dykes: Journal of Geophysical Research, v. 96, p. 10,049–10,077, doi:10.1029/91JB00600.

Ludwig, K.R., 2001, Squid, Version 1.02: A User's Manual: Berkeley Geochronology Center Special Publication 2, 21 p.

Mancktelow, N.S., 1990, The structure of the southern Adelaide fold belt, South Australia, *in* Jago, J.B., and Moore, P.S., eds., The Evolution of a Late Precambrian–Early Palaeozoic Rift Complex: The Adelaide Geosyncline: Geological Society of Australia Special Publication 16, p. 369–395.

Mancktelow, N.S., 2006, How ductile are ductile shear zones?: Geology, v. 34, p. 345–348, doi:10.1130/G22260.1.

McFadden, R.R., Teyssier, C., Siddoway, C.S., Whitney, D.L., and Fanning, C.M., 2010, Oblique dilation, melt transfer, and gneiss dome emplacement: Geology, v. 38, p. 375–378, doi:10.1130/G30493.1.

McKenzie, D., 1984, The generation and compaction of partially molten rock: Journal of Petrology, v. 25, p. 713–765, doi:10.1093/petrology/25.3.713.

McLellan, E.L., 1988, Migmatite structures in the Central Gneiss Complex, Boca de Quadra, Alaska: Journal of Metamorphic Geology, v. 6, no. 4, p. 517–542, doi:10.1111/j.1525-1314.1988.tb00437.x.

Offler, R., and Fleming, P.D., 1968, A synthesis of folding and metamorphism in the Lofty Ranges, South Australia: Australian Journal of Earth Sciences, v. 15, no. 2, p. 245–266.

Parrish, R.R., 1990, U-Pb dating of monazite and its application to geological problems: Canadian Journal of Earth Sciences, v. 27, no. 11, p. 1431–1450, doi:10.1139/e90-152.

Petford, N., Cruden, A.R., McCaffrey, K.J.W., and Vigneresse, J.L., 2000, Granite magma formation, transport and emplacement in the Earth's crust: Nature, v. 408, no. 6813, p. 669–673, doi:10.1038/35047000.

Rabinowicz, M., and Vigneresse, J.L., 2004, Melt segregation under compaction and shear channeling: Application to granitic magma segregation in a continental crust: Journal of Geophysical Research, v. 109, p. B04407, doi:10.1029/2002JB002372.

Robin, P.-Y., 1979, Theory of metamorphic segregation and related processes: Geochimica et Cosmochimica Acta, v. 43, p. 1587–1600, doi:10.1016/0016-7037(79)90179-0.

Rosenberg, C.L., and Handy, M.R., 2005, Experimental deformation of partially melted granite revisited: Implications for the continental crust: Journal of Metamorphic Geology, v. 23, no. 1, p. 19–28, doi:10.1111/j.1525-1314.2005.00555.x.

Rubin, A.M., 1993a, Dikes vs. diapirs in viscoelastic rock: Earth and Planetary Science Letters, v. 119, p. 641–659, doi:10.1016/0012-821X(93)90069-L.

Rubin, A.M., 1993b, Tensile fracture of rock at high confining pressure: Implications for dike propagation: Journal of Geophysical Research, v. 98, p. 15,919–15,935, doi:10.1029/93JB01391.

Rushmer, T., 2001, Volume change during partial melting reactions: Implications for melt extraction, melt geochemistry and crustal rheology: Tectonophysics, v. 342, p. 389–405, doi:10.1016/S0040-1951(01)00172-X.

Rutter, E.H., and Neumann, D.H.K., 1995, Experimental deformation of partially molten Westerly granite under fluid-absent conditions, with implications for the extraction of granitic magmas: Journal of Geophysical Research–Solid Earth, v. 100, p. 15,697–15,715, doi:10.1029/94JB03388.

Sandiford, M., Oliver, R.L., Mills, K.J., and Allen, R.V., 1990, A cordierite-staurolite-muscovite association, east of Springton, Mt. Lofty Ranges; implications for the metamorphic evolution of the Kanmantoo Group, *in* Jago, J.B., and Moore, P.S., eds., The Evolution of a Late Precambrian–Early Palaeozoic Rift Complex: The Adelaide Geosyncline: Geological Society of Australia Special Publication 16, p. 483–495.

Sandiford, M., Fraser, G., Arnold, J., Foden, J., and Farrow, T., 1995, Some causes and consequences of high-temperature, low-pressure metamorphism in the eastern Mt. Lofty Ranges, South Australia: Australian Journal of Earth Sciences, v. 42, no. 3, p. 233–240, doi:10.1080/08120099508728197.

Sawyer, E.W., 1994, Melt segregation in the continental crust: Geology, v. 22, no. 11, p. 1019–1022, doi:10.1130/0091-7613(1994)022<1019:MSITCC>2.3.CO;2.

Sawyer, E.W., 1996, Melt segregation and magma flow in migmatites: Implications for the generation of granite magmas: Transactions of the Royal Society of Edinburgh–Earth Sciences, v. 87, no. 1–2, p. 85–94, doi:10.1017/S0263593300006507.

Sawyer, E.W., 1998, Formation and evolution of granite magmas during crustal reworking: The significance of diatexites: Journal of Petrology, v. 39, no. 6, p. 1147–1167, doi:10.1093/petroj/39.6.1147.

Sawyer, E.W., 2001, Melt segregation in the continental crust: Distribution and movement of melt in anatectic rocks: Journal of Metamorphic Geology, v. 19, no. 3, p. 291–309, doi:10.1046/j.0263-4929.2000.00312.x.

Sawyer, E.W., 2008, Atlas of Migmatites: Canadian Mineralogist Special Publication 9, 371 p.

Sawyer, E.W., and Brown, M., 2008, Working with Migmatites: Mineralogical Association of Canada, Short Course Series 38, 158 p.

Schärer, U., 1984, The effect of initial ^{230}Th disequilibrium on young U-Pb ages: The Makalu case, Himalaya: Earth and Planetary Science Letters, v. 67, p. 191–204, doi:10.1016/0012-821X(84)90114-6.

Stern, R.A., and Berman, R.G., 2000, Monazite U-Pb and Th-Pb geochronology by ion microprobe, with an application to in situ dating of an Archean metasedimentary rock: Chemical Geology, v. 172, p. 113–130, doi:10.1016/S0009-2541(00)00239-4.

Stevenson, D.J., 1989, Spontaneous small-scale melt segregation in partial melts undergoing deformation: Geophysical Research Letters, v. 16, no. 9, p. 1067–1070, doi:10.1029/GL016i009p01067.

Tassone, D.R., 2008, Crustal Melting and Melt Extraction: The Role of Migmatites in the Evolution of the Southern Adelaide Fold-Thrust Belt [Honour's thesis]: Adelaide, Australia, University of Adelaide, 104 p.

Vanderhaeghe, O., 2001, Melt segregation, pervasive melt migration and magma mobility in the continental crust: The structural record from pores to orogens: Physics and Chemistry of the Earth, Part A, Solid Earth and Geodesy, v. 26, no. 4–5, p. 213–223, doi:10.1016/S1464-1895(01)00048-5.

Vanderhaeghe, O., 2009, Migmatites, granites and orogeny: Flow modes of partially-molten rocks and magmas associated with melt/solid segregation in orogenic belts: Tectonophysics, v. 477, p. 119–134, doi:10.1016/j.tecto.2009.06.021.

Vernon, R.H., 2004, A Practical Guide to Rock Microstructures: Cambridge, UK, Cambridge University Press, 594 p.

Vigneresse, J.-L., and Burg, J.P., 2000, Continuous vs. discontinuous melt segregation in migmatites: Insights from a cellular automaton model: Terra Nova, v. 12, p. 188–192, doi:10.1046/j.1365-3121.2000.00299.x.

Weinberg, R.F., and Mark, G., 2008, Magma migration, folding, and disaggregation of migmatites in the Karakoram shear zone, Ladakh, NW India: Geological Society of America Bulletin, v. 120, no. 7–8, p. 994–1009, doi:10.1130/B26227.1.

Weinberg, R.F., and Podlatchikov, Y., 1994, Diapiric ascent of magmas through power-law crust and mantle: Journal of Geophysical Research, v. 99, no. B5, p. 9543–9559, doi:10.1029/93JB03461.

Weinberg, R.F., and Regenauer-Lieb, K., 2010, Ductile fractures and magma migration from source: Geology, v. 38, no. 4, p. 363–366, doi:10.1130/G30482.1.

Weinberg, R.F., Mark, G., and Reichardt, H., 2009, Magma ponding in the Karakoram shear zone, Ladakh, NW India: Geological Society of America Bulletin, v. 121, no. 1–2, p. 278–285.

White, L. T., and Ireland, T. R., 2012, High-uranium matrix effect in zircon and its implications for SHRIMP U-Pb

age determinations: Chemical Geology, v. 306–307, p. 78–91.

Wickham, S.M., 1987, The segregation and emplacement of granitic magma: Journal of the Geological Society of London, v. 144, p. 281–297, doi:10.1144/gsjgs.144.2.0281.

Williams, I.S., and Hergt, J.M., 2000, U-Pb dating of Tasmanian dolerites: A cautionary tale of SHRIMP analysis of high-U zircon, *in* Woodhead, J.D., Hergt, J.M., and Noble, W.P., eds., Proceedings, Beyond 2000 New Frontiers in Isotope Geoscience, Lorne, January–February 2000: Melbourne, University of Melbourne, p. 185–188.

Williams, I.S., Buick, I.S., and Cartwright, I., 1996, An extended episode of early Mesoproterozoic metamorphic fluid flow in the Reynolds Range, central Australia: Journal of Metamorphic Geology, v. 14, p. 29–47, doi:10.1111/j.1525-1314.1996.00029.x.

Yassaghi, A., James, P.R., Flöttmann, T., and Winsor, C.N., 2004, *P-T* conditions and kinematics of shear zones from the southern Adelaide fold-thrust belt, South Australia: Insights into the dynamics of a deeply eroded orogenic wedge: Australian Journal of Earth Sciences, v. 51, no. 2, p. 301–317, doi:10.1111/j.1400-0952.2004.01059.x.

Science Editor: Christian Koeberl
Associate Editor: Roger Lawrence Gibson

Manuscript Received 4 September 2012
Revised Manuscript Received 31 January 2013
Manuscript Accepted 2 February 2013

Printed in the USA